Probing Charge Generation in 3D Photonic Poly(3-hexylthiophene)/Titanium Dioxide Nanocomposites for Bulk Heterojunction Solar Cells

Nicholas Tulsiram

A thesis submitted to

the faculty of graduate studies

in partial fulfillment of the requirements

for the degree of

Master of Science

Graduate Program in Chemistry

York University

Toronto, Ontario

March 2016

Abstract

Organic photovoltaics (OPVs) are attractive for their inexpensiveness, large-scale fabrication methods, flexibility and semi-transparency. OPVs have lower efficiencies than conventional inorganic semiconductor-based solar cells, and hence methods to enhance light-harvesting properties are sought-after. Photonic crystals are unique nanomaterials that present the ability to enhance light-harvesting properties through electromagnetic field localization and slow photon effect. In this work, three-dimensional photonic crystals were successfully integrated into the active layers of bulk-heterojunction solar cells by fabricating a series of titanium dioxide inverse opals coated with poly(3-hexylthiophene). The optical, morphological, and charge generation properties of the nanocomposites were investigated. Transient photoinduced absorption spectroscopy showed enhanced charge generation due to a potential photonic enhancement and the increased interfacial area of the porous structure. This research serves as a proof of concept, where the photonic properties of inverse opals and their high surface area may be exploited with different materials in other solar cell systems.

Acknowledgements

I would like to express my greatest thanks to Professor Jennifer Chen for providing me with the opportunity, guidance and support throughout my masters research. Since I arrived at York, Professor Chen has constantly challenged me, making me realize what I am truly capable of. The skills I have learned over the past 2 years are invaluable and will continue to guide and help me in all of my future endeavors. I thank her for allowing me to be a part of this amazing group.

I also thank all of my lab mates, past and present for making me feel welcome and providing me with a wonderful and unforgettable experience. Special thanks to Brian Malile for his support and help throughout my project as well as making those conference trips something to remember. I also thank Chris Kerr for helping me perform experiments and teaching me a lot about myself. I also thank all of the other Chen group members, Julia, Kim, Anthony, Josh, Elspeth and Rabia for their assistance and making lab much more entertaining.

I thank my committee members, Dr. Barry Lever, Dr. William Pietro and Dr. Simone Pisana for taking the time to read my thesis and providing feedback.

I would also like to thank Jerry Grech, Karen Rethoret, Sue Mamiche, and Joe Manion for all their assistance throughout my research.

Thank you to all of my friends for their unrelenting support and valuable advice. I appreciate all of them being there for me when I needed it most. Consuelo Perez, Cait Carew, Michelle Shuoprasad, Avmeet Virdi, Hasan Khan, Shan Kaushal and Ravneet Gill, thank you.

Finally, I thank my parents and my sister, Rebecca. Without them I would not be where I am today.

Table of Contents

List of Figures

CHAPTER 1

CHAPTER 2

CHAPTER 3

List of Tables

List of Schemes

List of Abbreviations

AFM	atomic force microscopy
AR	antireflection
a-Si	amorphous silicon
BHJ	bulk heterojunction
CdSe	cadmium selenide
CdS	cadmium sulfide
CdTe	cadmium telluride
CIGS	copper indium gallium arsenide
DSSC	dye-sensitized solar cell
EA	electroabsorption
EISA	evaporation induced self-assembly
EQE	external quantum efficiency
fcc	face-centered cubic
FTO	fluroine-doped tin oxide
GaAs	gallium arsenide
HE	high energy
HOMO	highest occupied molecular orbital
HTL	hole transport layer
ICBA	indene-C_{60} bisadduct
InGaAs	indium gallium arsenide
i-P3HT/TiO_2-o	inverse P3HT/titania opal
i-TiO_2-o	inverse titania opal

LE	low energy
LED	light-emitting diode
LUMO	lowest unoccupied molecular orbital
MEH-PPV	poly(2-methoxy-5-(2'-ethyl-hexyloxy)-1,4-phenylene vinylene)
MoO_3	molybdenum oxide
$mTiO_2$	mesoporous titanium dioxide/titania
OPV	organic photovoltaic
P3HT	poly(3-hexylthiophene)
PbS	lead sulfide
PCBM	[6,6]-phenyl-C61-butyric acid methyl ester
PIA	photoinduced absorption spectroscopy
PL	photoluminescence
PPV	poly(p-phenylenevinylene)
PTB7	poly[[4,8-bis[(2- ethylhexyl)oxy]benzo[1,2-b:4,5-b9]dithiophene-2,6-diyl][3-fluoro-2-[(2-ethylhexyl)carbonyl]thieno[3,4-b]thiophenediyl]]
PV	photovoltaic
QTH	quartz tungsten halogen
SEM	scanning electron microscopy
SWA	scalar-wave approximation
$Ti(OBut)_4$	titanium (IV) butoxide
TiO_2	titanium dioxide/titania
UV-vis	ultraviolet-visible
ZnO	zinc oxide

CHAPTER 1

Introduction

1.1 Organic Photovoltaics

1.1.1 Background

Solar energy is a renewable, environmentally-friendly and highly abundant energy source that has the potential to contribute a greater proportion of the global energy demand. The sun strikes the earth with approximately 96000 TW of power in one hour, however, only a small fraction of that energy can be captured.[1] The amount of solar energy that can be harvested is restricted by three major factors: 1) the sunlight that that strikes land is easily obtainable compared to the sunlight that strikes the sea, 2) the land available for solar array installations is limited and 3) the Shockley-Queisser limit places the maximum power conversion efficiency of a single junction solar cell at approximately 30%.[2] Assuming a 1% coverage of the lands surface (1.48 million km^2) with solar cells operating at 10% efficiency, approximately 245500 TWh of energy could be generated in a year, which is approximately 1.5 times greater than the total world energy consumption in 2014 (155714 TWh).[1,3] While this scenario may seem promising, the inherent challenge is developing a cost-efficient way to convert the available solar energy to electricity. To assess the economic value of an energy source, a variety of factors must be taken into consideration. The two main factors include the cost of building and operating a power generating plant with respect to the power generated over its lifetime and the costs associated with implementing the technology to the grid with respect to the power it supplies. To be considered economically viable, the cost of building and operating a plant must be lower than the costs needed to implement the technology.[4]

While the current costs associated with implementing solar photovoltaics are comparable to that of other power generating technologies[4], there are significantly high costs associated with building, operating and maintaining a solar photovoltaic power generating plant. In order to become economically viable over the long term, significant reductions in cost need to be made. The short-term energy outlook by the Energy Information Administration (EIA) reports an average 1% decline in power generation by natural gas and coal by the year 2017, while hydropower is expected to rise to 1% and other renewables 2% by the year 2017.[5] Although there is a slow decline in the power production share of fossil fuels, the relative cheapness and high energy output enables it to remain as the dominant energy provider for at least the next 30 years.[6,7] Of the renewable energies, solar photovoltaic technology is the fastest growing energy source at a rate of 6.8% per year (in the US).[8,9] This growth can be seen in the rapid development of new solar cell technologies over the past 6 years as shown in figure 1.1.[10]

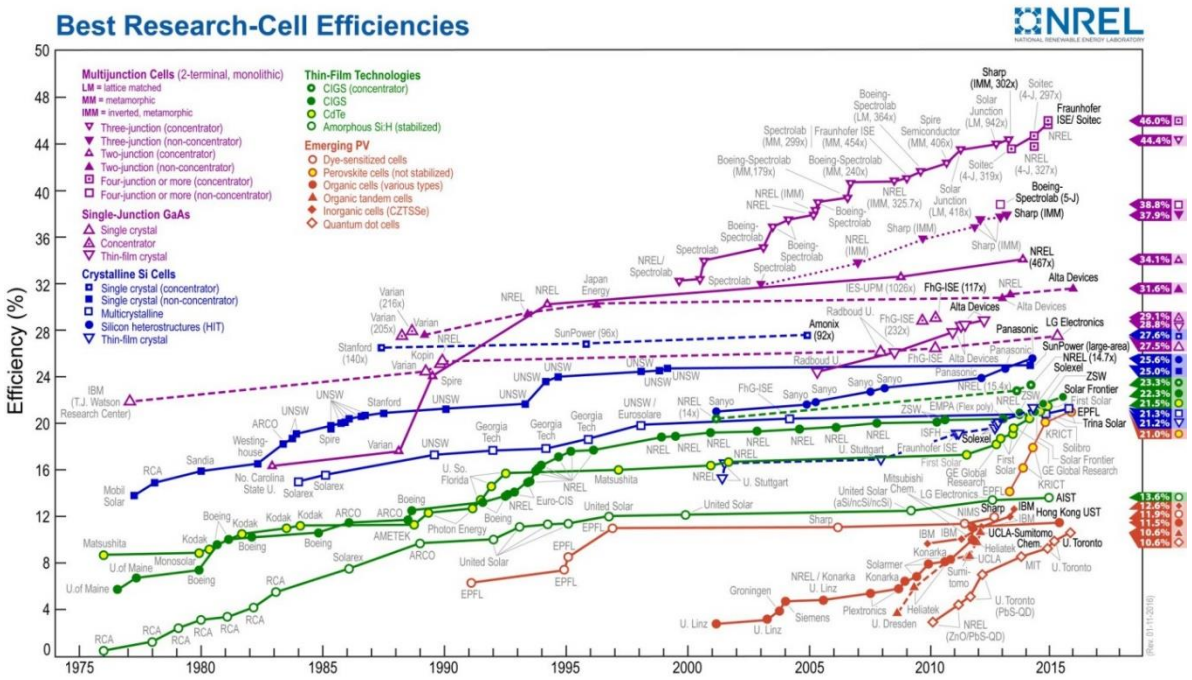

Figure 1.1. Best research-cell efficiencies reported over time by the National Renewable Energy Laboratory (NREL). Purple, blue, green and red data lines represent multijunction cells, crystalline Si cells, thin-film technologies and emerging PV technology (including organic photovoltaics), respectively. Reprinted from ref. [9].

Currently, the majority of the utility-scale solar energy market are dominated by crystalline silicon (Si), gallium arsenide (GaAs), cadmium telluride (CdTe) and copper indium gallium diselenide (CIGS) based devices.[11] These technologies have produced high-performing modules with efficiencies of 22.9, 24.1, 17.5 and 17.5% as of July 2014.[12] Although these modules are highly efficient, the materials needed to fabricate them are expensive. Organic solar cells, also known as organic photovoltaics (OPVs), are an alternative solar cell technology that has received great interest due to the low costs associated with the materials and fabrication processes. OPVs use materials that are solution-processable enabling production on large scales using methods such as inkjet and screen printing as well as roll-to-roll processing.[13,14] While the

low-cost materials and large-scale fabrication methods are desirable for solar cell production, OPVs possess significant limitations preventing widespread use. These limitations include low power conversion efficiencies, short operational lifetimes and variations in devices, which ultimately increases overall costs.[11] The highest reported module efficiency of an organic solar cell is 8.7% by Toshiba, which is well below the 10% efficiency demand in order to be considered for commercialization.[12,15] Despite the low efficiencies of these devices, other advantages of OPVs such as their flexibility, transparency, light weight and low-light performance can serve a variety of other applications.[16] Some of the major applications are low-powered consumer electronics such as portable chargers, phones and tablets.[9] In addition, OPVs have potential in developing countries where its affordability and low maintenance are advantageous in areas where access to power is scarce.[17,18] OPVs can also be integrated into textile applications such as uniforms, backpacks and tents making them desirable for military purposes such as recharging batteries for equipment.[1] Future potential applications for organic photovoltaics are building-integrated photovoltaics, where solar panels are installed as roofs, windows or into the walls of buildings. Currently, amorphous silicon (a-Si) solar cells are widely in use due to their availability, non-toxicity, long lifetime and robustness.[19] In order to be integrated in private or commercial buildings, the efficiencies and long-term stabilities of OPVs would need significant improvement while maintaining low costs.

The wide variety of organic materials available, provide many possibilities for the development of organic-based devices. The poly(3-hexylthiophene) (P3HT)/[6,6]-phenyl-C_{61}-butyric acid methyl ester (PCBM) blend has been extensively studied and has consistently produced devices with efficiencies ranging from 2 to 5%.[14] There has also been extensive research in the development of alternative donor and acceptor materials such as poly[[4,8-bis[(2-

ethylhexyl)oxy]benzo[1,2-b:4,5-b9]dithiophene-2,6-diyl][3-fluoro-2-[(2-ethylhexyl)carbonyl]thieno[3,4-b]thiophenediyl]] (PTB7) and indene-C_{60} bisadduct (ICBA), respectively which have led to high performing devices.[20,21] The versatility of organic materials enable devices with different configurations to be developed. One such type of device is the tandem solar cell which has led to devices with high power conversion efficiencies.[22,23] Tandem devices take advantage of multiple active layers to absorb different parts of the solar spectrum which reduce thermodynamic energy losses.[23] Small molecule donors are also an area of research, as they can be easily reproduced and purified providing reliable analyses of structure-property relationships.[24] Recently, a solution-processable small molecule based donor was employed in devices producing efficiencies up to 6.7%.[25] The growing development of OPVs will continue to produce new organic materials for high performing devices, increasing the possibility for widespread commercialization.

1.1.2 Bulk Heterojunction Solar Cells

Initial OPV designs were based on a bilayer structure comprised of two organic materials. The photogeneration of charges were produced at the interface of the two layers each with specific electron or hole transport properties. In 1986, Tang reported a bilayer OPV using phthalocyanine and perylene derivatives producing efficiencies of 1%.[26] This concept was expanded upon by Heeger *et al.* in 1995, with the introduction of a bulk heterojunction solar cell made from blending the conductive polymer, poly(2-methoxy-5-(2'-ethyl-hexyloxy)-1,4-phenylene vinylene) (MEH-PPV) with the fullerene derivative, PCBM, producing device efficiencies of 2.9%.[27] Bulk heterojunction (BHJ) solar cells are excitonic solar cells based on the concept of ultrafast electron transfer. The main component in a BHJ solar cell is the active

layer which is a mixture of donor and acceptor materials phase-separated with nanoscale morphology. The low ionization energy of the donor combined with the high electron affinity of the acceptor enables the transfer of electrons. The most common materials are conjugated polymers and fullerene derivatives as the donor and acceptor materials, respectively.

The generation of charge from a bulk heterojunction depends on the successful dissociation of charge carriers at donor-acceptor interfaces and subsequent transport of charges through the active layer to separate electrodes.[28] The processes of charge generation in a BHJ solar cell are shown in figure 1.2.

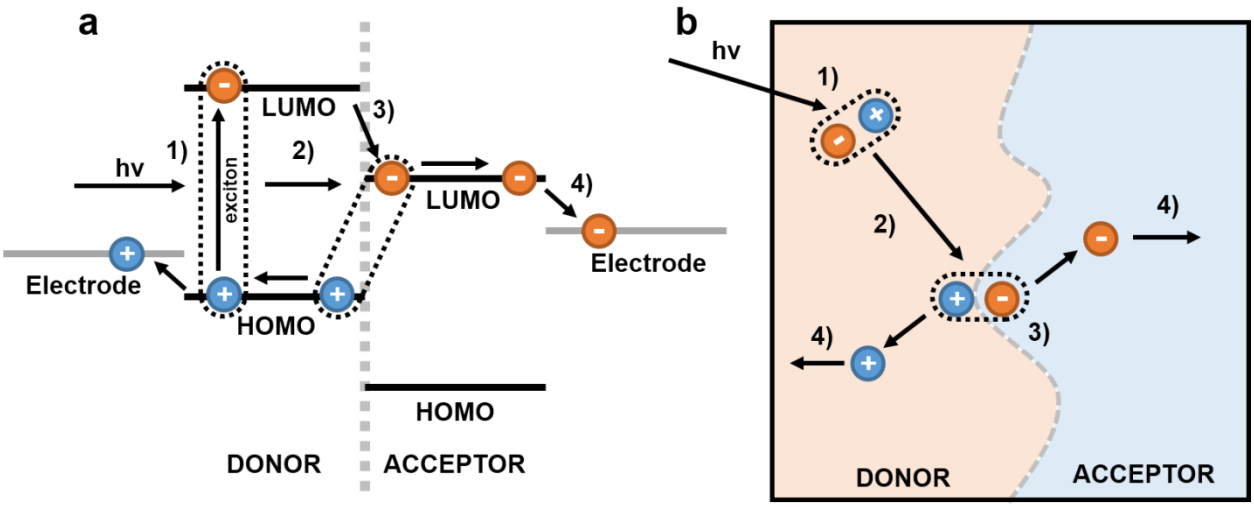

Figure 1.2. **S**implified energy diagram of an organic BHJ system outlining the processes required for charge generation (a) with the corresponding processes shown at a donor-acceptor interface (b). Blue and orange circles represent holes and electrons, respectively. The dotted black and grey lines represents the Coulombic attraction between the charge carriers and donor-acceptor interface, respectively.

The production of charges requires the photoexcitation of the active layer, which excites an electron from the highest occupied molecular orbital (HOMO) to the lowest unoccupied

molecular orbital (LUMO) in the donor material (1). As a result, a Coulombically-bound electron-hole pair, known as an exciton, is formed. The exciton can diffuse to a donor-acceptor interface (2) where electron transfer to the acceptor will take place (3). To achieve the successful transfer of an electron into the LUMO of the acceptor, the exciton must be within the diffusion length of an interface, which range from 5 to 15 nm in conjugated polymers.[29] In addition, the transfer must be energetically favourable and the energy difference between the LUMO of the donor and acceptor materials must be greater than the Coulombic attraction of the exciton to initiate charge separation.[30] The separated electron and hole will be transported through the acceptor and donor, respectively, and collected at the electrodes (4). The difference in the work functions of the electrodes are responsible for providing a driving force for the direction in which the charge carriers are transported.[28]

The morphology of the active layer has been extensively studied to maximize the production of charge carriers while minimizing losses due to the recombination of free charge carriers. The nature of the donor-acceptor interface and the ordering of the two phases play a significant role in the production and transport of charge carriers. The majority of control over the active layer lies in the processing conditions. Some of these factors include the solvent from which the active layer is cast, the ratio of the donor and acceptor components in the film, the molecular structure of the components, controlling the rate of phase separation through thermal or solvent annealing as well as the addition of chemical additives to modify the interface between the two phases.[31–33] In a study by Li *et al*., a variety of different P3HT/PCBM films were produced under different processing conditions to observe the effect on device performance.[34] Figure 1.3 shows experimental atomic force microscopy (AFM) height images of the morphologies of active layers produced under different conditions.

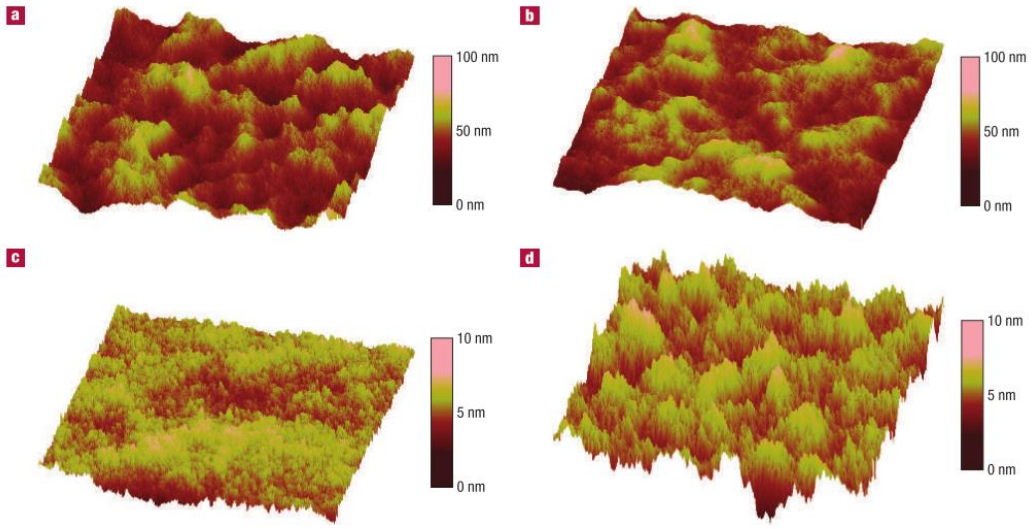

Figure 1.3. AFM height images of P3HT/PCBM active layers displaying the effect of a slow grown (a), slow grown and annealed (b), fast grown (c) and fast grown annealed (d) active layer. Note the difference in scale bars. Image reprinted with permission from Macmillan Publishers Ltd: Nature Materials ref. [33], copyright 2005.

The images compare the difference between a fast and slow grown film and the effect of annealing on these films. The annealed slow grown films were found to produce the most efficient devices where the AFM images indicated that the rough structure of the film was characteristic of a highly ordered blend. The increased ordering of the phases in the blend translated to greater absorption properties and increased mobilities of charge carriers.[34] It is therefore highly advantageous to develop ways to control the morphology and interface of the active layer to improve the charge generation and transport properties.

1.1.3 Hybrid Organic-Inorganic Donor-Acceptor Systems

The use of inorganic materials as the acceptor provides greater control over the morphology of the active layer in comparison to a purely organic blend. A controlled

morphology provides greater insight towards charge kinetics in comparison to a randomly mixed active layer, which can be difficult to reproduce and characterize. Inorganic acceptors offer multiple advantages over organic acceptors, such as the ability to tune the microstructure of the acceptor phase, decreased Coulombic binding energies of excitons due to the high dielectric constant, increased active layer absorption and enhanced electron mobility.[35–38]

A commonly used inorganic hybrid system includes conjugated polymers with nanoparticles such as cadmium selenide (CdSe), cadmium sulfide (CdS) or lead sulfide (PbS). These nanoparticles can display high absorption to complement the absorption of the donor material and thus enhance device efficiencies.[36,39] In addition, the shape and domain size of nanoparticles can enhance charge separation and transport. Large ordered crystalline domains of the nanoparticles result in charge delocalization enhancing the dissociation of excitons at interfaces (Fig. 1.4), while nanorods 30 nm in length facilitate charge dissociation and transport due to the decreased number of inter-particle hops.[35–37,40]

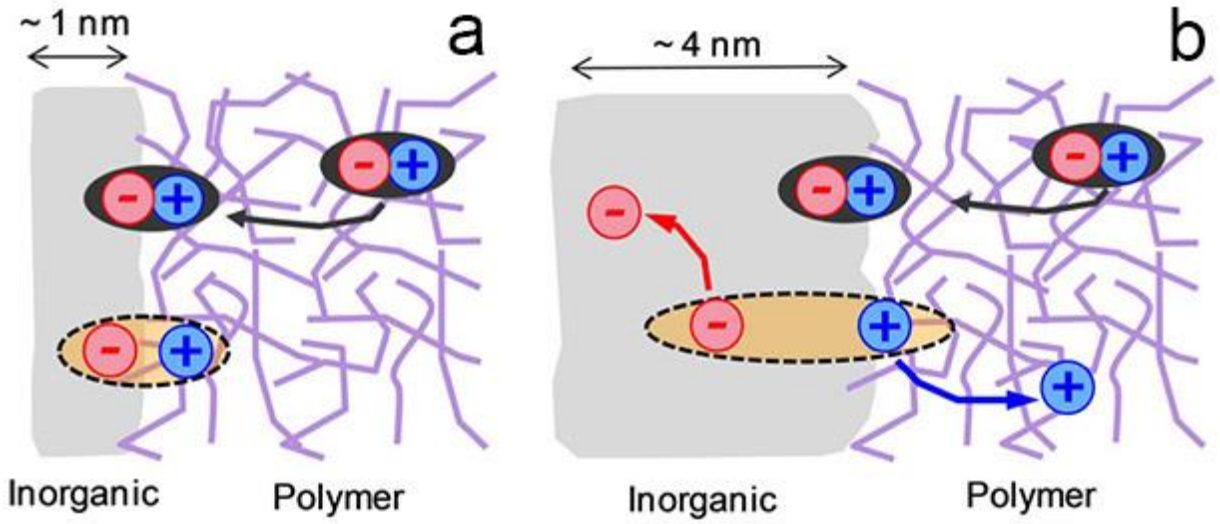

Figure 1.4. Diagram outlining the effect of inorganic domain size and the effect on charge delocalization. A smaller inorganic domain (a) results in closely bound excitons, while larger domains enables the delocalization of the electron facilitating exciton dissociation (b). Image adapted with permission from Nature Publishing Group: Scientific Reports ref. [34], copyright 2013.

Oxide-based semiconductors have also been used as the acceptor material owing to their abundance, low toxicity, chemical stability and high electron mobilities.[38,41] Metal-oxides can also be fabricated into a variety of structures via simple synthetic processes. For example zinc oxide (ZnO) nanowires were readily fabricated through vacuum and solution-based methods.[41] More complex and reproducible structures were also fabricated such as nanobelts and nanohelices.[42] Titanium dioxide (TiO_2) acceptors have been extensively studied where efficient electron injection into the conduction band has been observed when coated with semiconductive polymers such as MEH-PPV and poly(*p*-phenylenevinylene) (PPV).[43] Optimization studies employing the use nanotube arrays, surface modification and modification of the TiO_2 pore sizes have also been investigated, to enhance charge transport and increase the polymer interface.[44–47]

Inorganic materials offer a high degree of structural control which have benefited the development of light-manipulating nanostructures.

1.2 Optical Enhancements in PVs

The manipulation of light in photovoltaic systems is a strategy for enhancing and controlling light absorption. Thin film PVs use less material which reduces weights and thicknesses, ultimately reducing overall costs. Thinner active layers benefit from increased probabilities of exciton dissociation due to the comparable lengths of the active layer thickness and exciton diffusion. The reduced active layer thickness, however, leads to incomplete photon absorption which hinders device efficiencies.[48] The development and incorporation of photonic nanostructures in thin films have thus become a viable method to enhance the photon absorption efficiency, while maintaining thin devices.

Common light-manipulating nanostructures for thin film applications include antireflection (AR) layers, gratings, scattering structures, plasmonics and photonic crystals. One method to enhance light absorption is to reduce the amount of light that is reflected by the surface of the solar cell using an AR layer. This can be achieved using multiple layers that vary from the refractive index of air to the substrate, which reduces the abrupt change in refractive index which causes the reflection of light.[19] Figure 1.5 shows an example of a graded-index AR layer.

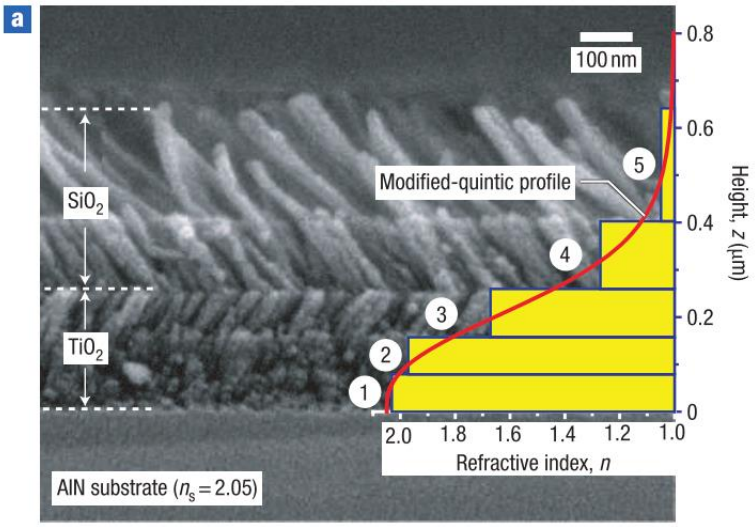

Figure 1.5. Cross sectional SEM image of a graded index AR coating comprised of five layers with varied refractive indices (shown by yellow bars). Height of the coating is shown to the right. Image reprinted with permission from Macmillan Publishers Ltd: Nature Photonics ref. [48], copyright 2008.

Xi *et al.*, fabricated AR coatings from TiO_2 and SiO_2 nanorods using oblique-angle deposition.[49] The AR coating possesses a gradual change from the refractive index of air to the aluminum nitride substrate and was able to successfully reduce the reflection of light to 0.5% for wavelengths between 574 to 1010 nm.

Gratings, surface structures, scattering structures and waveguides are often used to enhance absorption. These structures are able to scatter, diffract and guide light in order to increase the effective optical path length which increases the probability of absorption.[50] Plasmonics and photonic crystals are two versatile structures that possess similar abilities. Plasmonics study the optical properties of metallic nanostructures. These nanostructures give rise to surface plasmons, which are optically induced oscillations of electrons at the surface of the metal.[51] Surface plasmons are able to concentrate, trap and scatter light which make them

highly desirable for thin film photovoltaics which can provide a versatile route to enhance absorption.[52] Figure 1.6 shows multiple light-trapping methods using metal nanostructures.

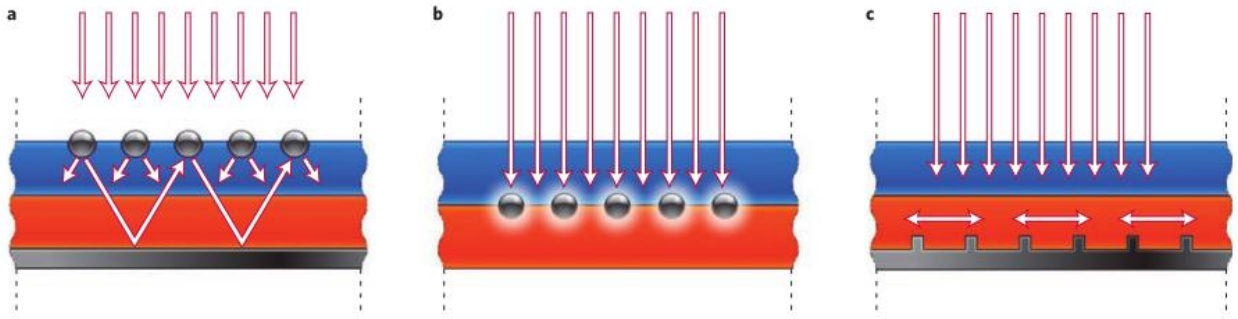

Figure 1.6. Light trapping methods using metal nanoparticles embedded at the surface of the solar cell to scatter light (a), within the semiconducting layer to promote the generation of electron-hole pairs (b) and a corrugated metal back surface to trap light (c). White arrows represent the direction of light. Reprinted with permission from Macmillan Publishers Ltd: Nature Materials ref. [52], copyright 2010.

Light can be effectively scattered and/or concentrated through the use of metal nanoparticles embedded at the surface or within the substrate. Nanoparticles at the surface scatter light, increasing the optical path length and thus enhances absorption.[53] When embedded in the semiconducting layer, the field generated by the surface plasmons promotes the production of electron-hole pairs.[53] A corrugated metal back surface has the ability to trap light via the excitation of surface plasmon polaritons at the metal-semiconductor interface.[53]

Metallic nanoparticles of a certain shape or size have been demonstrated to strongly enhance electromagnetic fields near the nanoparticle when excited by a specific wavelength of light.[52] This occurs due to localized surface plasmon resonance where an optical excitation induces the collective oscillations of electrons near the surface of the nanoparticle.[54] The high near-field intensities will result in enhanced absorption of the surrounding material. Plasmon-

enhanced solar cells have been extensively studied where increased efficiencies were attributed to the presence of nanoparticles embedded within the devices.[55] Photonic crystals also demonstrate enhanced absorption due to the localization of the electromagnetic field of light. They are periodic dielectric structures that produce stop bands – a range of wavelengths where light is forbidden to propagate through the crystal in a certain direction. Wavelengths above and below this forbidden range will be localized on a specific material in the crystal which can enhance the absorption properties of the material. The fundamentals of photonic crystals are discussed in Chapter 2.

1.3 Applications of Photonic Crystals

The unique photonic properties of photonic crystals make them interesting materials for a variety of light-dependent applications. The incorporation of photonic crystals in OPVs have garnered much attention, specifically in dye-sensitized solar cells (DSSC). DSSCs make use of a photoactive dye coupled to a semiconductor oxide to generate charge, where the dye is regenerated through the use of an electrolyte.[56]

Tétrault *et al.* employed a double layer DSSC with a mesoporous TiO_2 underlayer and a TiO_2 inverse opal on top depicted in figure 1.7.[57]

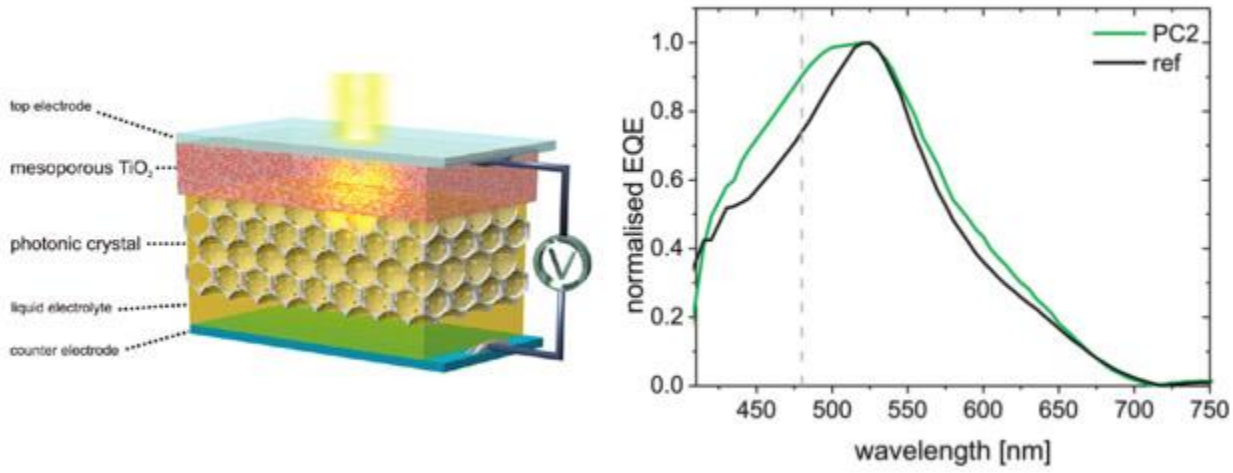

Figure 1.7. Schematic of the photonic crystal-DSSC architecture with the external quantum efficiency spectrum of one of the photonic crystals used in the study. Green and black lines represent the spectrum of the photonic crystal device and reference device, respectively. Dashed grey line shows the position of the stop band. Adapted with permission from ref. [56]. Copyright 2010 American Chemical Society.

This type of configuration allowed for effective dye sensitization, electrolyte infiltration and efficient charge collection from both layers. Three different inverse opals each with a different photonic stop band position were tested and produced an increase in the external quantum efficiency (EQE) corresponding to the positions of the respective stop bands.[57] The increased EQE was attributed to the effects of light localization and light with reduced group velocities or slow photons observed at the red edge of the stop band.

Photonic crystals have also been used for photocatalytic experiments. Chen *et al.* demonstrated the enhanced photocatalytic degradation of adsorbed methylene blue on nanocrysalline TiO_2 inverse opals due to slow photons.[58] This enhancement was achieved by determining the optimal slow photon energy that corresponded to the electronic bandgap of TiO_2.

Under monochromatic light at the optimized energy, slow photons were effectively harvested, which translated to a two-fold increase in the photo-oxidation rate.[58]

The slow photon enhancement has also increased the photoconductivity of silicon solar cells demonstrated by Suezaki *et al*. Silicon inverse opals were used, which produced a complete photonic bandgap owing to the high dielectric contrast between silicon and air.[59] The charge transport of the silicon inverse opal was improved via crystallization and hydrogen-plasma passivation in combination with the structure of the inverse opal.[60] In addition, the electrical properties of silicon inverse opals were evaluated and shown to correlate with the photonic band gaps.[61] Boron and phosphorous doped silicon inverse opals have also been synthesized where the electrical conductivities were improved in comparison to an undoped silicon inverse opal.[62] The combined electrical and photonic properties of the doped inverse opals have proven to be useful for solar cell applications.

1.4 Motivation and Objective

The goal of this project is to successfully integrate a photonic crystal into a polymer-based photovoltaic system to investigate the feasibility of the slow photon enhancement for increasing efficiencies. A bulk heterojunction architecture will be used where P3HT and a TiO_2 inverse opal will act as the donor and acceptor phase, respectively. The TiO_2 inverse opal will yield a large, highly ordered interface which will increase the probability of charge generation when combined with P3HT. In addition, the continuous network of TiO_2 in combination with its high dielectric constant can aid with charge screening and reduce recombination. A series of inverse opals with different periodicities were fabricated and spin-coated with P3HT to yield the nanocomposite. Photoinduced absorption spectroscopy (PIA) was used to determine the number

and lifetimes of polarons generated under blue and green excitation. Polaron generation is compared across the series to elucidate any photonic enhancements that may arise due to slow photons. This research serves as a proof of concept to determine the possible optical enhancements due to the presence of the TiO_2 inverse opal photonic crystal, which can then be applied to other materials in different systems.

CHAPTER 2

Fabrication and characterization of opal templates and inverse opals

2.1 Photonic crystals

2.1.1 Background

The concept of a photonic crystal was first realized independently by Yablonovitch and John in 1987.[63,64] They proposed using periodic dielectric structures to control the photonic properties of the material. Yablonovitch and John found that a periodic dielectric structure was able to change the radiative properties of the material[63] and localize photons on different parts of the structure.[64] Photonic crystals are highly ordered and periodic structures made from two different dielectric materials on the length scale of light.[65] These unique structures can be found in nature and are responsible for the iridescent colours seen in butterfly wings, opal gemstones and in the skin of chameleons.[66–68]

Photonic crystals can be made from virtually any solid material in variety of designs. These crystals are classified by the number of dimensions where periodicity of the dielectrics is observed: 1, 2 and 3D photonic crystals (Fig 2.1).[69]

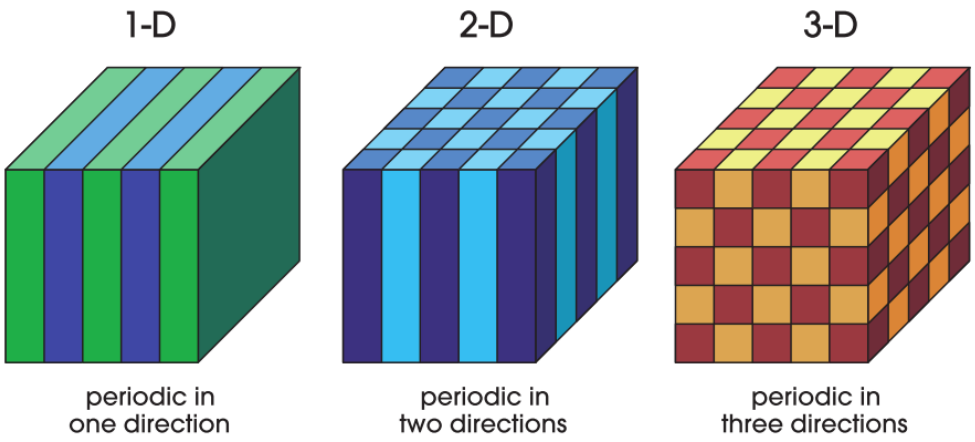

Figure 2.1. Schematic showing the different types of photonic crystals and the arrangement of the dielectric media. The colours represent materials with different dielectric constants in each system. Reprinted from ref. [68]. Copyright 2008 Princeton University Press.

One dimensional photonic crystals are the simplest type of photonic crystal and consist of a multilayer film with repeating layers of two dielectrics.[69] This type of photonic crystal is also known as a Bragg mirror where light with specific wavelengths are reflected. Two dimensional photonic crystals are commonly organized as a square array of rods in a different dielectric media. These crystals are commonly used for waveguiding and light localization through the use of point defects within the structure.[70]

2.1.2 Three-dimensional Photonic Crystals

Three dimensional photonic crystals have periodicity in three directions and can be easily fabricated using sub-micron colloidal spheres.[66] A synthetic opal film can be obtained through evaporation induced self-assembly (EISA), where the spheres in solution will self-assemble onto a substrate in a face-centered cubic (fcc) arrangement with (1 1 1) lattice planes parallel to the substrate.[71] These opal templates can then be used to fabricate another type of 3D photonic

crystal known as an inverse opal. The opal film is used as a template, where the voids of the film are filled with another material of interest. Common materials of interest include inorganic oxides and semiconducting materials where metal alkoxide precursors are used to fill the voids via infiltration or chemical vapour deposition.[72]

Opal and inverse opal films display colours similar to those found in nature. These colours occur due to the constructive interference of light from the diffraction and refraction of light according to Bragg's law (1.1) and Snell's law (1.2).

$$n\lambda = 2d \sin\theta \qquad 1.1$$

$$\frac{n_1}{n_2} = \frac{\sin\alpha}{\sin\beta} \qquad 1.2$$

Light incident on the (1 1 1) planes of the photonic crystal will be diffracted by the lattice points in the crystal as well as refracted due to the refractive index of the photonic crystal, as shown in figure 2.2.

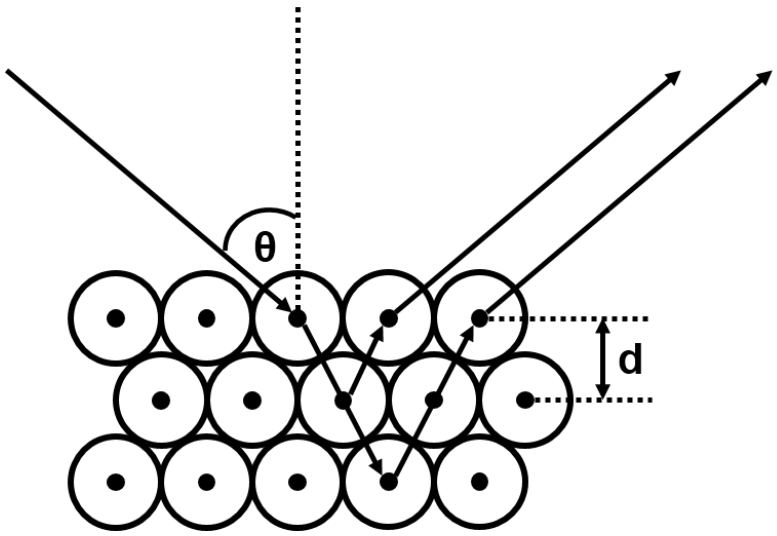

Figure 2.2. Depiction of the Bragg diffraction and refraction of light due to the (1 1 1) planes of a photonic crystal. Specific wavelengths of light will be reflected only if constructive interference is observed.

The reflected wavelengths of light can be predicted by modifying Bragg's law with Snell's law to take into account the refraction of light. The modified form of Bragg's law can be obtained by equating the angle, θ, to the angles described in Snell's law. The modified Bragg equation also takes into account the effective refractive index of the photonic crystal and is defined as

$$n\lambda = 2d\sqrt{n^2{}_{eff} - sin^2\theta} \qquad 1.3$$

Where *n* refers to the order of the stop band, *d* is the interplanar distance between the (1 1 1) lattice planes, θ is the angle between the incident beam and the normal of the film and n_{eff} is the effective refractive index of the crystal:

$$n_{eff} = f n_{sphere} + (1 - f) n_{void} \qquad 1.4$$

Where *f* refers to the filling fraction of the face-centered cubic structure ($f = 0.74$) and n_{sphere} and n_{void} refer to the refractive indices of the sphere and void materials, respectively.

2.1.3 Photonic Properties of Photonic Crystals

Photonic crystals have the ability to manipulate and control the flow of photons similar to how semiconductors are able to control the flow of electrons.[65] Depending on the dielectric contrast between the two materials and periodicity, a phenomenon known as a photonic band gap will arise. Similar to a band gap in a semiconductor, a photonic band gap is a range of wavelengths that are forbidden to propagate through the crystal in all directions.[69] Photonic crystals with a complete photonic band gap have been demonstrated most notably by Blanco *et al*. who fabricated a silicon inverse opal with a band gap centered at 1.46 μm.[59] Figure 2.3 shows an SEM image of the Si inverse opal and the theoretical band diagram.

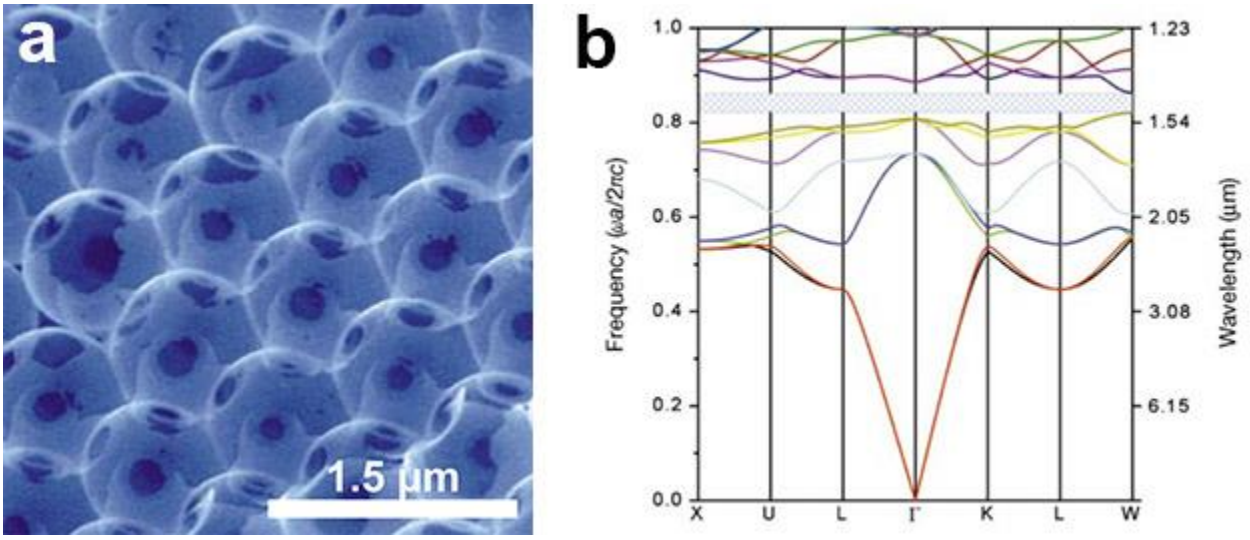

Figure 2.3. SEM image of the (1 1 1) internal facet of the Si inverse opal (a) with the theoretical photonic band diagram with respect to wavevector, assuming 88% Si infiltration (b). The shaded region indicates the photonic band gap. Image adapted with permission from Macmillan Publishers Ltd: Nature ref. [58], copyright 2000.

The high refractive index of Si (3.45) in contrast to the refractive index of air (1) enables the formation of a photonic band gap. The photonic band diagram, plotted in terms of frequency of light with respect to the Brillouin zone, describes the propagation of light within the photonic crystal. A Brillouin zone refers to the allowed wavevectors in a specific region where the bands present in each region indicates the allowable frequencies of light in each zone.[65] A common occurrence seen in photonic crystals is the presence of a photonic stop band. A stop band is a range of frequencies where light is unable propagate through the crystal in a specific direction.[58] A stop band can be observed in the photonic band diagram in figure 2.4 for the Γ – L region at approximately 2.5 µm. The stop bands will produce Bragg peaks in the reflection spectrum, as these regions prohibit the propagation of light throughout the crystal, shown in figure 2.4.

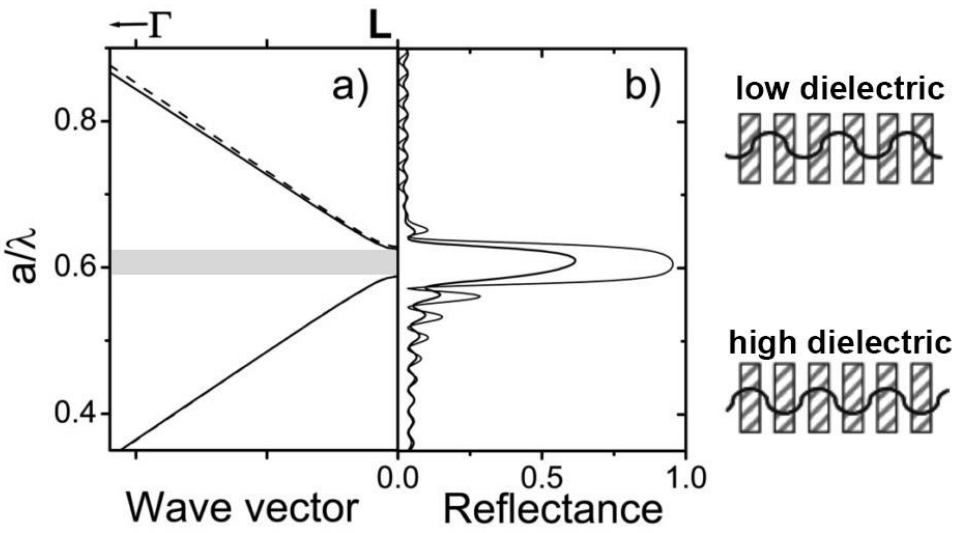

Figure 2.4. Theoretical band diagram for a polystyrene opal in the Γ – L Brillouin zone (a) and the corresponding reflectance spectrum (b). Energy is represented in reduced frequency units where a represents the lattice constant and λ represents the wavelength of light in a vacuum. Shaded region represents stop band (a). Thick and thin lines (b) represent experimental and theoretical reflectance spectra, respectively. Image adapted with permission from ref. [79] Copyright 2003 by the American Physical Society.

Photonic crystals also exhibit the ability to localize light on different parts of the crystal. At each edge of the photonic stop band, there exists two wavelength regions of light that are able to propagate through the crystal. These two wavelength regions are spatially shifted with respect to each other where the electromagnetic waves are localized on a specific material in the photonic crystal.[73] At wavelengths to the blue edge of the gap, light is localized on the low dielectric medium, while frequencies towards the red edge of the gap correspond to light localized on the high dielectric medium.[74] The degree of localization depends on the dielectric contrast where a greater contrast will increase the confinement of light to one material.[75]

In addition to the localization of the electromagnetic field of light, photonic crystals are able to reduce the group velocity of light. The group velocity refers to the speed at which the envelope of light propagates through space.[75] The photonic band diagram reveals the flattening of bands at the edges of a photonic stop band or bandgap.[76] This corresponds to light with a group velocity of zero where light is fully reflected. Light with reduced group velocity, also known as slow photons, would therefore have an increased effective optical path length and result in an increased interaction with the medium.[58,76] The reduced group velocity of light in combination with the localization of the electromagnetic field further improves the usefulness of photonic crystals for light harvesting applications.

2.2 Experimental

Inverse opal nanocomposites were fabricated using a template method. Scheme 2.1 depicts the three-stage process: 1) the fabrication of an opal template; 2) the formation of a TiO_2 inverse opal; and 3) spin-coating a polymer onto the inverse opal. The templates, inverse opals and inverse opal nanocomposites were characterized using various techniques to ensure the samples were of high quality.

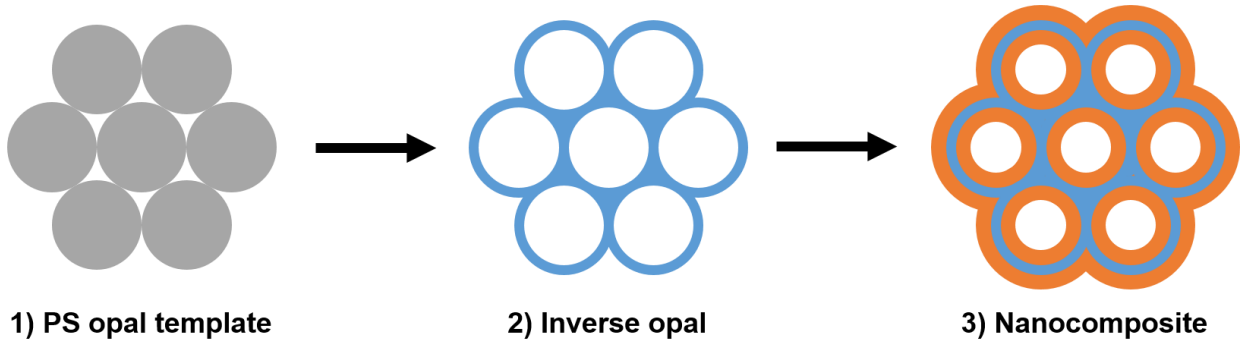

Scheme 2.1. Outline of the three main steps involved to fabricate the photonic nanocomposite. The grey circles, the blue outline and the orange shell represent the polystyrene spheres, TiO_2 inverse opal structure and P3HT coating, respectively. Drawing represents small portion of the highly repetitive structure.

2.2.1 Synthesis of polystyrene spheres

Polystyrene spheres with diameters of 140, 177, 224, 265, 320 and 375 nm were synthesized via surfactant-free emulsion polymerization.[77] A three-necked round-bottom flask was cleaned thoroughly and filled with 100 mL of Milli-Q water and 15 mL of ethanol. The remaining necks were stoppered with a bubbler attachment and the flask was placed into an oil bath at 75.8°C. While stirring, the solution was purged with nitrogen for 1 hour. After purging, approximately 5.05 g of styrene monomer, 100 to 400 µL of styrene sulfonate and 0.06 g of initiator were added to the solution. The size of the sphere was controlled by the amount of styrene sulfonate added. The initiators consisted of either 4,4′-azobis(4-cyanovaleric acid) or ammonium persulfate, depending on the desired sphere size. . The mixture was left to stir overnight under nitrogen atmosphere. The solution was cooled to room temperature and filtered with glass wool.

2.2.2 Opal Template Deposition

Opal templates were deposited onto glass substrates via EISA. Glass substrates were first cut to size and rinsed with water. The cut slides were then placed in piranha solutions of 3:1 sulfuric acid, hydrogen peroxide for 1 hour. The piranha solution was decanted and the slides were rinsed six times and stored in a beaker with Milli-Q water. Glass slides were dried and rinsed with isopropanol and then suspended vertically in shell vials containing 6 mL solutions of ethanol and polystyrene spheres. The thickness of the opal template depended on the volume fraction of spheres in the solution where greater volume fractions of spheres resulted in thicker films. The solution with the suspended slide was placed in an oven at 55°C for 2 days to yield the opal template.

2.2.3 Inverse Opal Fabrication

TiO_2 inverse opals were fabricated by infiltrating opal templates with sphere diameters ranging from 140 nm to 375 nm and number of layers ranging from 7 to 30, with titanium (IV) butoxide ($Ti(OBut)_4$). Opal templates were suspended vertically in a solutions of ethanol containing 0.4 to 1.1 vol% of $Ti(OBut)_4$ in a desiccator under vacuum. The rate of evaporation was controlled using a needle valve. The $Ti(OBut)_4$ filled the voids present in the opal template as the ethanol solution evaporated, where the titanium precursor hydrolyzed to yield amorphous TiO_2. The inverse opals were calcined at 450°C for 4 hours to burn off the opal template yielding anatase TiO_2 in the inverse opal structure.

2.2.4 Preparation of P3HT Solution

The polymer used in this study was P3HT. A reference donor material, PCBM, was also used. Materials were weighed out in a glovebox under argon atmosphere. P3HT solutions of approximately 16 mg/mL were made by dissolving the polymer in an appropriate amount of chlorobenzene and the solution was stirred for 3 hours at 70°C. To make P3HT/PCBM mixtures, equal volumes of each individual solution were mixed together and stirred for an additional 3 hours.

2.2.5 Preparation of Mesoporous TiO_2 Films

A reference mesoporous TiO_2 ($mTiO_2$) film was prepared via sol-gel method. First, $Ti(OBut)_4$ was added to a vial containing hydrochloric acid while stirring. A second solution containing Pluronic P123 dissolved in 1-butanol was prepared. The second solution was then added to the first. The combined solution was left to stir for 2 hours where it was then spin coated onto cleaned glass substrates for 20 seconds at 2400 rpm. The coated glass substrates were placed in a humidity chamber for 2 days to promote hydrolysis. The films were then calcined at 450°C for 4 hours to yield a transparent, uniform film of TiO_2 in the anatase phase.

2.2.6 Spin Coating of Polymer on Inverse Opal

Glass substrates, $mTiO_2$ films and inverse opals (approximately 1.3 cm by 1.3 cm) were coated with P3HT in this study. Mesoporous TiO_2 films and inverse opals were coated with 100 and 50 µL, respectively, of the polymer solution and spin-coated at 1000 rpm for 2 minutes. P3HT/PCBM samples were prepared by spin coating 50 µL of the mixed P3HT/PCBM solution onto cleaned glass substrates. The samples were stored under vacuum in the dark.

2.2.7 Scanning Electron Microscopy (SEM)

Scanning electron microscopy (SEM) images were taken using a FEI Quanta 3D dual-beam FEG FIB operating at 10 to 20 kV. Samples of inverse opals and inverse opal nanocomposites on glass were attached onto aluminium holders using carbon tape. An additional piece of carbon tape was attached from the sample to the holder to prevent charging. Samples were mounted inside the microscope and images were obtained under 0.30 Torr at working distances of 7 to 10 mm using a low vacuum secondary electron detector.

2.3 Results and Discussion

2.3.1 Optimization and Structural Characterization of Opal Template Films

To fabricate high quality nanocomposites, various film deposition conditions were tested to determine the best condition to produce opal templates. Glass substrates were suspended in vials containing polystyrene-ethanol mixtures and placed in three different locations: atop a lab bench, in a fumehood and in an oven at 60°C. Film were left to deposit for 6, 4 and 1 days, respectively. Opal templates obtained from the fumehood and lab bench had multiple variations in the film due to vibrations from the surroundings, with the number of layers ranging from 10 to 12 layers. Opal templates deposited in the oven resulted in high quality uniform films but were also thin with approximately 10 layers. To reduce the amount of variations in film quality and increase thicknesses of the films, depositions were performed in the oven at a reduced temperature of 55°C. Upon evaporation of the ethanol solution, the polystyrene spheres self-assembled in a fcc orientation with (1 1 1) planes parallel to the surface of the substrate, yielding the high quality opal templates seen in figure 2.5. In addition, the number of layers could be

carefully controlled by adjusting the temperature within 10°C of 55°C. Herein, opal templates are referred to by the opal sphere diameter determined by simulated scalar wave approximations.

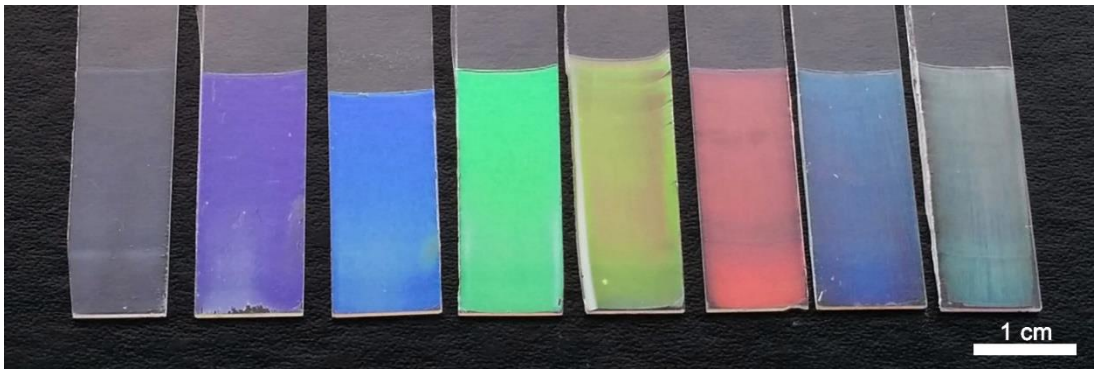

Figure 2.5. Photograph of opal templates made from polystyrene sphere diameters of 140, 177, 200, 224, 245, 265, 320 and 375 nm (left to right).

SEM images were taken to determine the polydispersity of the synthesized polystyrene spheres. To obtain high quality uniform opal templates, it is critical that polystyrene spheres are of low polydispersity to ensure the packing into the fcc structure. Any deformities in the polystyrene spheres will disrupt the packing and produce an irregular film. A diluted sample of the polystyrene spheres was deposited onto a glass slide for characterization. Figure 2.6, reveal spheres with an average diameter of 229 nm and standard deviation of 6 nm.

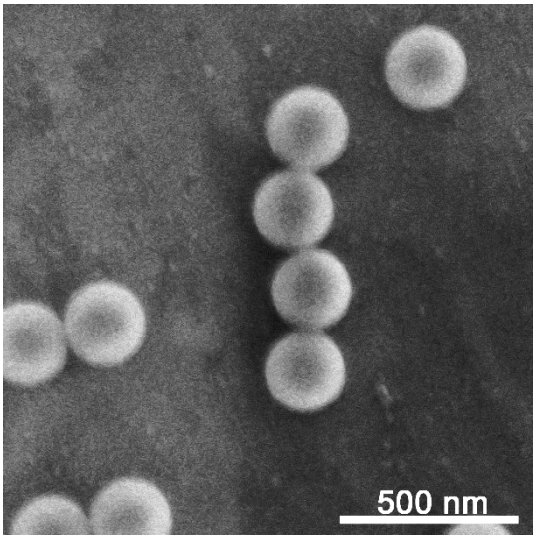

Figure 2.6. SEM image of 224 nm diameter polystyrene spheres with low polydispersity.

2.3.2 Reflectance Measurements of Opal Templates

Reflectance spectra of the opal templates were obtained using a microscope equipped with a spectrometer to determine the position of the stop bands. The reflectance spectra displayed the stop bands with Fabry-Perot fringes on opposite sides of the peak, which arise due to the constructive interference of light from the reflections at the top and bottom surfaces of the opal (Fig. 2.7).[78] The presence of the fringes indicate the high quality of the samples with the number of fringes proportional to the number of layers in the sample.[79] The sphere diameter and number of layers can be fitted using scalar-wave approximation (SWA) simulation software.

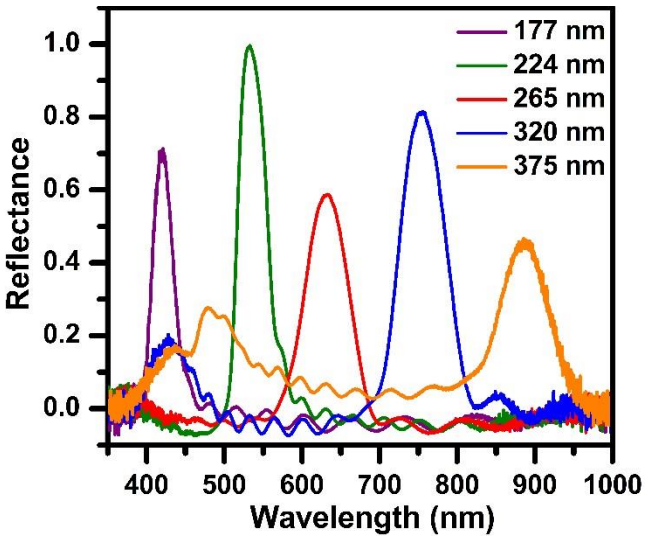

Figure 2.7. Reflectance spectra of polystyrene opal templates with different sphere diameters (labelled in legend) determined via SWA simulations. Stop band positions shift to longer wavelength with increasing polystyrene sphere diameters.

SWA neglects the polarization of light and only takes into account the scattering of light in high symmetry directions of the crystal.[79,80] The simulation provides the interplanar spacing as well as the number of lattice planes in the crystal, which allow for the determination of the diameter of the sphere and number of layers, respectively.[80] Figure 2.8, shows an example of the fitting of experimental data to the simulated SWA data. The sphere diameter obtained from SWA modelling is close to that from SEM imaging (224 nm vs 229 ± 6 nm).

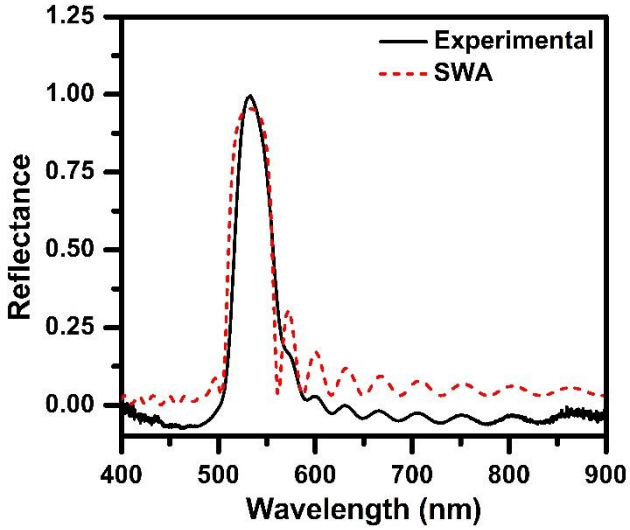

Figure 2.8. Reflectance spectra of an opal template with a PS sphere diameter of 224 nm. (solid black line) The simulated SWA data (dashed red line) is shown assuming a sphere diameter of 224 nm with 22 layers.

2.3.3 Structural Characterization of Inverse Opals

To obtain a structurally sound inverse opal structure, the infiltration process was also optimized. The amount of $Ti(OBut)_4$ used to infiltrate the opal templates was based on the sphere diameter. The amounts of $Ti(OBut)_4$ were adjusted accordingly depending on the degree of film infiltration. Under-infiltrated films did not have enough $Ti(OBut)_4$ to fill the voids in the template and resulted in incomplete inverse opal structures (Fig. 2.9a). Over-infiltrated films contained an excess of titanium butoxide within in the ethanol solution and produced a layer of TiO_2 on top of the inverse opal which introduced additional sources of light scattering (Fig. 2.9b).

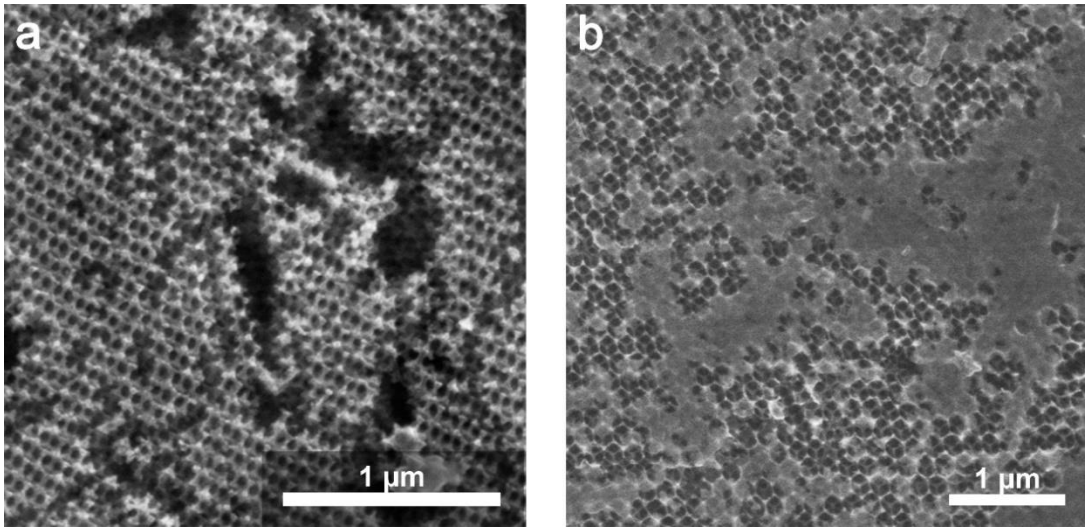

Figure 2.9. Examples of inverse opals that were under- (a) and over-infiltrated (b). The incomplete filling of the voids of the opal template results in a disordered and incomplete inverse opal while the excess filling of the opal template results in an over layer, scattering light.

Figure 2.10 shows the SEM images of a high quality inverse opal. The images reveal the presence of the fcc arrangement of the air spheres produced from the opal template used.

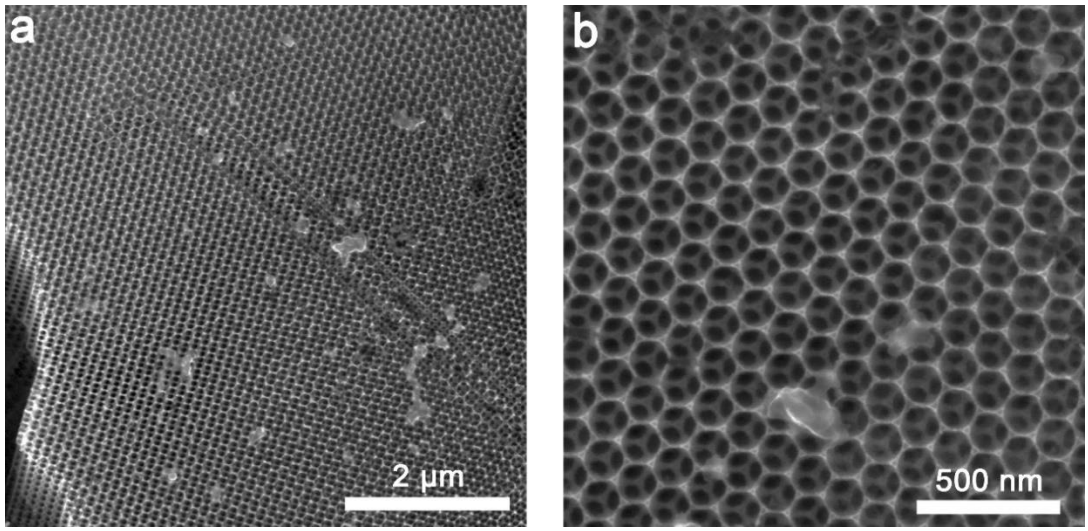

Figure 2.10. SEM images of a TiO_2 inverse opal made from a 140 nm opal template (a) and close up (b). The highly ordered and periodic structure of the inverse opal can be observed in the close up.

The quality of the inverse opal structure was affected by the thickness of the film. Films ranging from 15 to 25 layers produced high quality opals that were suitable for experiments, as thinner films have a greater number of defects in the sample. Defects in the inverse opals will result in unwanted wavelengths of light either being reflected or transmitted through the inverse opal which have been found to broaden and reduce the peak intensity.[81] Three types of defects were commonly seen in the structures of inverse opals shown in figure 2.11.

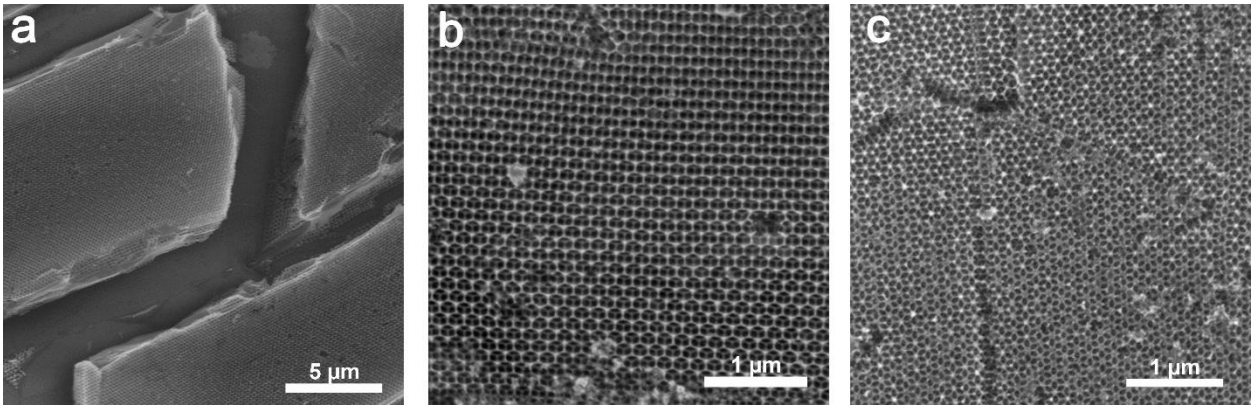

Figure 2.11. Types of defects seen in inverse opal structures: cracks (a), point (b) and line defects (c).

The most common defect seen was cracking in the film (Fig. 2.11a), which occured due to the shrinkage of the film from the hydrolysis and condensation reactions during the infiltration and calcination processes. These cracks were present in all inverse opals and are unavoidable for this type of fabrication method. Despite the presence of cracks, the orientation of the resulting inverse opal domains were maintained.

Point and line defects were also two common defects seen in the inverse opals to varying degrees (Fig. 2.11b,c). These defects arise during the self-assembly of the opal template and are transferred over during the inversion process. Although these defects distort the periodicity of

the inverse opal and are expected to affect the photonic properties, the photonic stop bands are observable with significant intensity.

Air sphere diameters of the inverse opal were measured from the SEM images and compared to the diameters of the polystyrene sphere in the opal template. The majority of inverse opal air spheres were approximately 80% of the original polystyrene sphere diameter. Inverse opals made from opal templates larger than 300 nm had air spheres 90% of the polystyrene sphere diameter. Shrinkage of the spherical voids occurred due to the drying of the film during the infiltration and calcination steps.

2.3.4 Structural Characterization of Inverse Opal Nanocomposites

Images of the inverse opals and inverse opal nanocomposites reveal the open structure of the inverse opal, shown in figure 2.12. After spin coating the inverse opal structure remains porous indicating that the P3HT coats the TiO_2 walls rather than produce a layer on top or completely fill the voids. The open structure ensures that the photonic properties of the inverse opal are preserved.

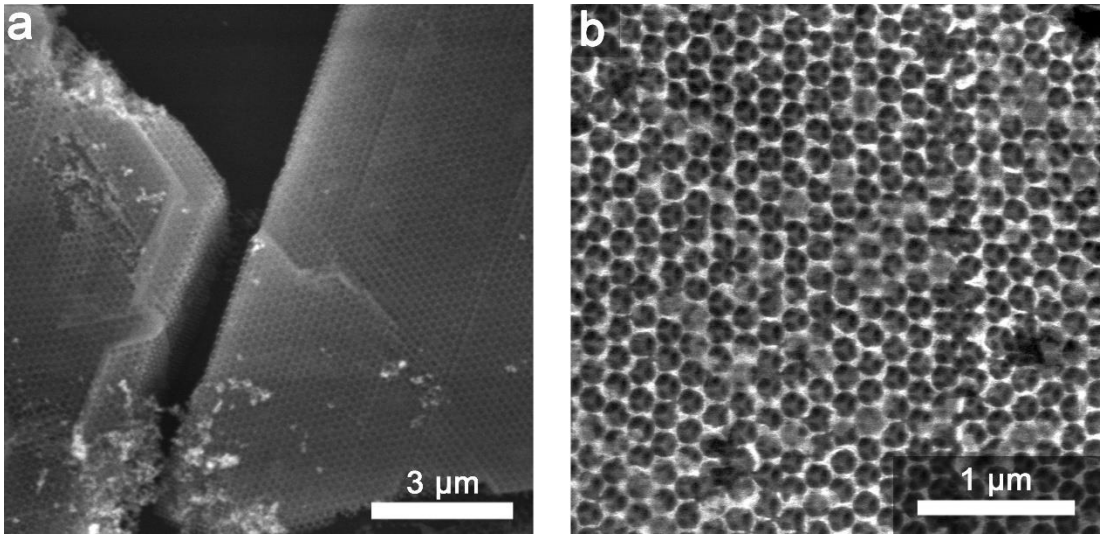

Figure 2.12. SEM images of nanocomposites after the spin coating process. Close up view (b) shows the open structure of the inverse opal is intact, allowing for the dielectric contrast to remain.

2.3.5 Optical Characterization of Inverse Opals

UV-visible (UV-vis) reflectance spectroscopy equipped with an integrating sphere was used to obtain diffuse reflectance measurements to determine the photonic stop band position of each inverse opal in the series. The integrating sphere enables the accurate measurement of all light reflected by the inverse opal accounting for any scattered light. The series of inverse opals used in this study had stop bands centered at approximately 300, 330, 360, 400, 440 and 540 nm (herein the prefix before i-TiO_2-o and i-P3HT/TiO_2-o indicates the photonic stop band position for inverse opals and inverse opal nanocomposites, respectively). Well-defined and intense peaks are indicative of high quality inverse opals. Figure 2.13 shows the diffuse reflectance spectra of the series of inverse opals measured in air and in water.

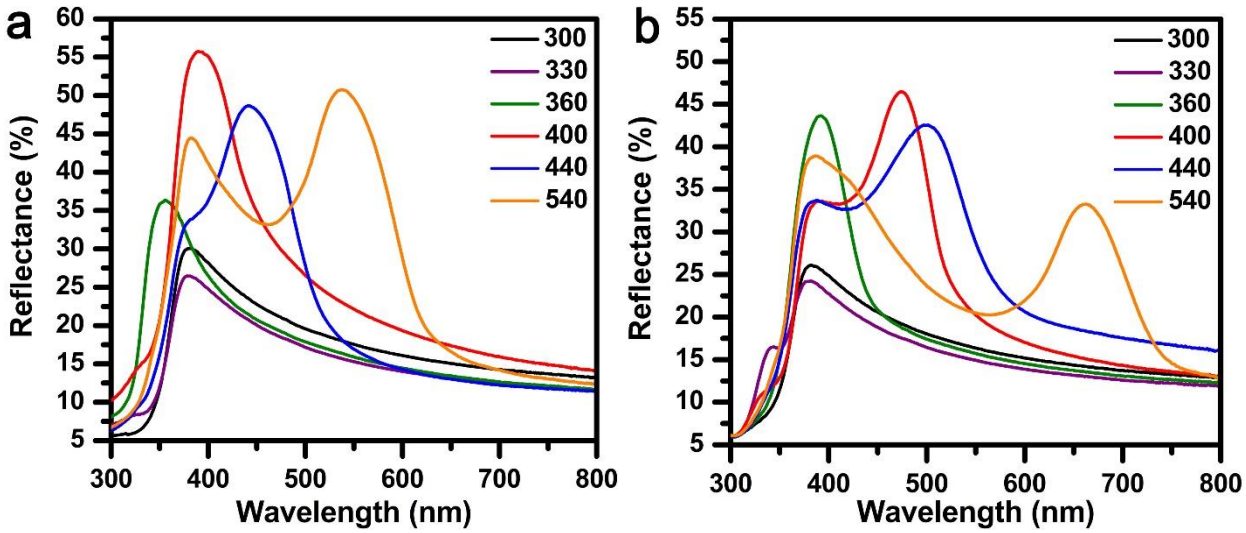

Figure 2.13. Diffuse reflectance spectra of TiO_2 inverse opals in air (a) and in water (b). Numbers in legends refer to the stop band position of each inverse opal measured in air. Spectra of the same colour correspond to the same sample measured in air or water.

The 300-i-TiO_2-o, without any observable photonic effects, displays a gradual increase in reflectance from 800 to 400 nm due to Rayleigh scattering. At wavelengths below 400 nm, there is a drastic decrease in diffuse reflectance due to the absorbance of UV light by TiO_2. The larger 400-, 440- and 540-i-TiO_2-o display defined stop band reflectance peaks. The intensity of the 360-i-TiO_2-o stop band is reduced because of the overlap with the absorbance of UV light by TiO_2. The 330-i-TiO_2-o stop band can be observed as a small bump in the spectrum at approximately 330 nm but is almost completely attenuated by the UV absorption of TiO_2.

Photonic stop bands of the inverse opals were also observed to red shift with increasing size of the sphere template. The red shift of stop bands can be explained by the modified Bragg's law (equation 1.3) where the interplanar distances, d, of the (1 1 1) planes of each inverse opal are directly proportional to the stop band position. Increasing the distance between

planes will result in longer wavelengths of light being constructively interfered, resulting in the red-shifting of the stop band.

To confirm the presence of the photonic properties, diffuse reflectance measurements were taken with the inverse opals submerged in water. Submerging the inverse opals in water fills the voids with water and results in an overall increase in the effective refractive index. According to the modified Bragg's law (equation 1.3), an increase in the effective refractive index will red shift of the stop band as seen in figure 2.13b. The red shift of the stop bands in the UV region enables these peaks to be distinguished from the absorption of UV light by the TiO_2. The red-shift of the 330-i-TiO_2-o and 360-i-TiO_2-o stop bands results in intensified peaks, as they are less suppressed by the UV absorption of TiO_2, which make the stop bands easily observable compared to the spectra in air. In contrast, the stop bands of the remaining inverse opals decrease in reflectance due to the decreased dielectric contrast between TiO_2 and water.

Table 2.1 summarizes the size of the opal template with the corresponding inverse opal stop band position in air, submerged in water and after coating with P3HT. The 300-i-TiO_2-o stop band was difficult to locate due to the high UV absorption of TiO_2 and was estimated based on the relative diameters of the other opal templates and their respective inverse opal stop band positions.

Table 2.1. Sphere diameter of the opal template and the photonic stop band positions of each inverse opal in air, water and the corresponding i-P3HT/TiO_2-o, with standard error of the mean reported. Label of i-TiO_2-o by stop band position are the approximate stop band positions used to identify the inverse opals.

Polystyrene opal template sphere diameter (nm)	**Label of i-TiO_2-o by stop band position (nm)**	**Average i-TiO_2-o stop band position in air (nm)**	**Average i-TiO_2-o stop band position in water (nm)**	**Average i-P3HT/TiO_2-o stop band position (nm)**
140	300	-	-	-
177	330	337 ± 5	368 ± 11	324 ± 2
224	360	358 ± 1	399 ± 3	363 ± 1
265	400	400 ± 3	452 ± 3	394 ± 1
320	440	444 ± 4	551 ± 10	437 ± 6
375	540	538 ± 2	635 ± 16	537 ± 1

2.3.6 Optical Characterization of Inverse Opal Nanocomposites

Optical characterization of the i-P3HT/TiO_2-o were also performed. Figure 2.14 shows the diffuse reflectance (a) and absolute absorbance (b) spectra of the inverse opals after spin coating with P3HT. All absorbance spectra (Fig. 2.14b) were normalized to the shoulder at 605 nm to compare the photonic effects in the shorter wavelength region (< 540 nm).

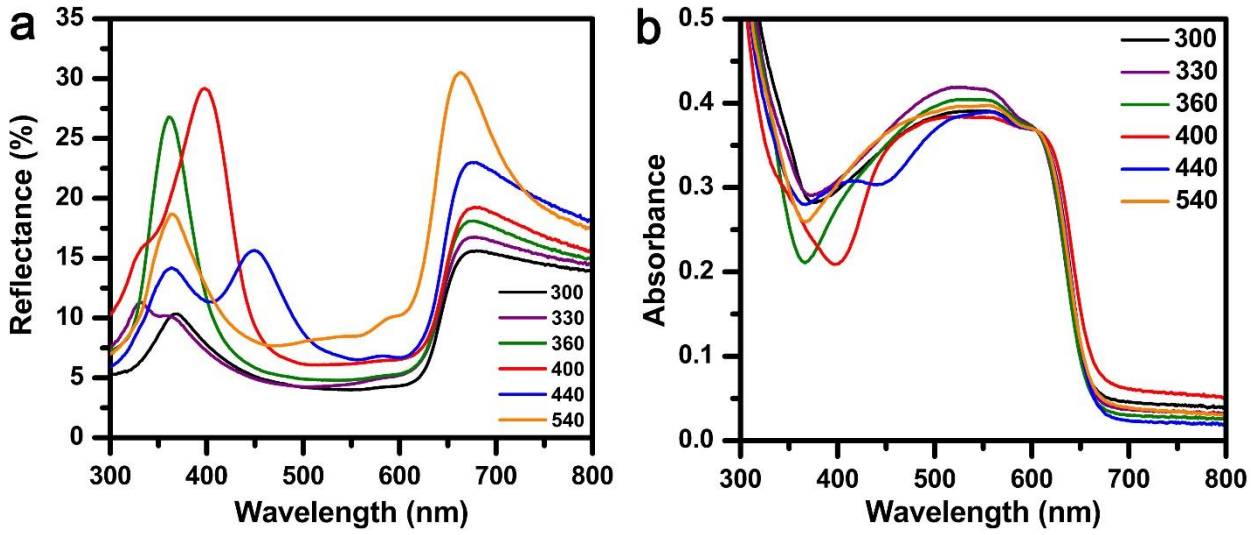

Figure 2.14. Diffuse reflectance (a) and absolute absorbance (b) of the i-P3HT/TiO_2-o obtained using an integrating sphere. Absolute absorbance spectra are normalized to the shoulder at 605 nm to compare changes in the P3HT absorbance due to photonic effects.

The reflectance spectra (Fig. 2.14a) reveal the preservation of the photonic properties of the inverse opals after spin coating. The coating of P3HT causes a significant decrease in the reflectance from 400 to 650 nm across all nanocomposites due to the high absorption of the polymer. The 300-i-P3HT/TiO_2-o, which does not exhibit any photonic properties, displays the lowest amount of random scattering. The 360-, 400- and 440-i-P3HT/TiO_2-o stop bands are still detectable but with reduced stop band intensities in comparison to the uncoated inverse opal. The stop band of 440-i-P3HT/TiO_2-o is suppressed more strongly because of the overlap of its energy with the onset of the P3HT absorption. The absorption of the P3HT leads to the almost complete suppression of the 540-i-P3HT/TiO_2-o stop band, where no peak is present. Highly absorbing materials have been previously shown to suppress photonic properties.[82] However, it should be noted that the reflectance between 400 and 600 nm is higher (at ~9%) for 540-i-

P3HT/TiO_2-o compared with other inverse opals suggesting some existence of stop band reflection near this region.

The photonic effects on the absolute absorbance of the i-P3HT/TiO_2-o are seen in figure 2.14b. The reflectance from the stop band is seen as a dip in the absorbance spectrum for most inverse opals. For example, a dip in the absorption spectrum at 366, 398 and 445 nm correspond to the stop bands of the 360-, 400- and 440-i-P3HT/TiO_2-o, respectively. A small dip in absorbance is observed for the 440-i-P3HT/TiO_2-o as its stop band is near the onset of P3HT absorption. The stop band of 540-i-P3HT/TiO_2-o is significantly suppressed by the absorption of the P3HT which does not show a well-defined dip arising from the photonic structure; instead, a slight reduction in absorption is seen from 450 to 550 nm, flattening the absorption peak. A sharp rise in absorption, relative to the other nanocomposites, is seen for the 400-i-P3HT/TiO_2-o in the 450 to 550 nm range, which may be attributed to slow photon enhancement. At the red edge of the stop band, the electromagnetic field of light is localized on the high dielectric material, TiO_2. Since the TiO_2 is coated with P3HT, the slow photons will have an increased interaction with the P3HT, which causes the enhanced absorption.

The modified Bragg's law states that the position of the stop band is related to the angle of the incident beam (θ). An increase in the angle of incident light will result in a blue-shift in the stop band. To confirm the photonic properties of the i-P3HT/TiO_2-o nanocomposites, absolute absorbance measurements were obtained at different angles of incident light. Figure 2.15 shows the absolute absorbance measurements of the 400-i-P3HT/TiO_2-o taken at four different angles to observe the shift of the stop band.

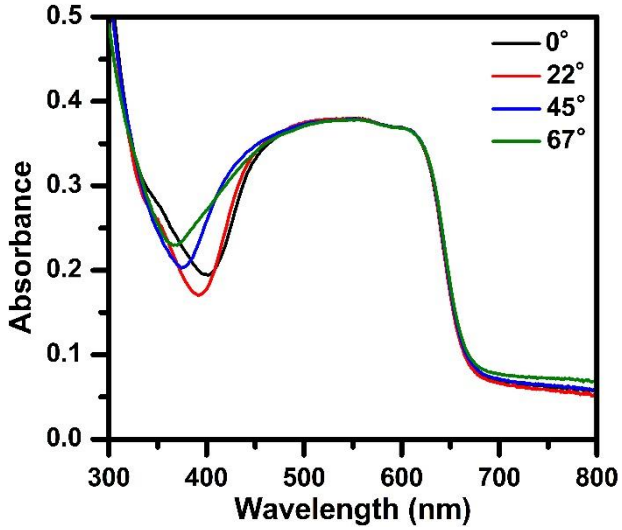

Figure 2.15. Absorbance spectra of a 440-i-P3HT/TiO_2-o at different incident angles obtained with an integrating sphere. The stop band initially centered at approximately 400 nm blue-shifts as the angle between the incident beam with respect to the normal of the film increases.

At 0° the stop band is positioned at 400 nm and as the incident angle is increased a blue shift is seen until 90° is met. Table 2.2 outlines the position of the stop band with respect to the angle of incidence.

Table 2.2. Positions of the 400-i-P3HT/TiO_2-o stop band corresponding to the angle of incidence with respect to the normal of the film.

Angle of incidence (°)	Stop band position (nm)
0	401
22	392
45	374
67	370

For comparison, absolute absorbance of control films of a P3HT, P3HT/PCBM and P3HT/mTiO_2 films were also obtained to compare the effects of the inverse opal on the absorbance of P3HT (Fig. 2.16).

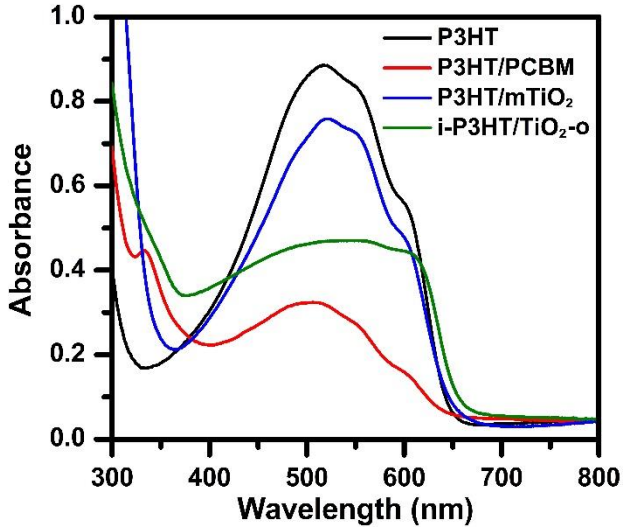

Figure 2.16. Absolute absorbance spectra of the reference films in comparison to 300-i-P3HT/TiO_2-o. The spectral shape of the 300-i-P3HT/TiO_2-o differs significantly from the reference films.

Regioregular P3HT tend to self-organize into planar sheets via inter-chain stacking, where films that are highly ordered will possess increased interactions between the planes and chains of P3HT.[31,34] The increased interactions will promote conjugation and result in lower energy optical transitions compared to P3HT films with more disorder.[83] The neat P3HT film, which is highly ordered, reveals the presence of absorption peaks at 519 attributed to the S_0 to S_1 transition with shoulders at 556 nm (A_2) and 605 nm (A_1) due to interactions between (interchain) and within P3HT chains (intrachain), respectively.[31,83–85] In comparison, the absorption features of the P3HT/PCBM film are slightly blue-shifted, because the PCBM domains disrupt the packing of the P3HT planes. Charge transfer between the P3HT and PCBM

domains has also been observed to modify the absorption of P3HT/PCBM blends.[83] The absorption of the P3HT/mTiO_2 bilayer closely resembles the spectrum of the pure P3HT film, with the addition of the high TiO_2 UV absorption below 350 nm. The lack of any significant modification to the absorption profile of the P3HT shows that the P3HT chains are well-ordered with a high degree of inter-chain interaction in a bilayer structure.[31,86]

On the other hand, the absorbance of the i-P3HT/TiO_2-o differs significantly from the neat P3HT film, where a more prominent A_1 absorption feature and higher relative absorption at shorter wavelengths (< 450 nm) is seen. The theoretical model of weakly interacting H-aggregates states describes the photophysics of neat P3HT films[87] and may provide some insight towards the morphology of P3HT on an inverse opal. H-aggregates refer to the parallel orientation of P3HT planes, where the monomer units are relatively aligned with each other.[87] The increased absorption at wavelengths below 420 nm for the i-P3HT/TiO_2-o is characteristic of unaggregated molecules or chains with shorter conjugation.[88] This indicates that the structure of the inverse opal may disrupt the packing of the P3HT planes causing a reduction in conjugation length. In contrast to the P3HT film, the A_1 absorption is much more prominent with respect to the A_2 absorption for the i-P3HT/TiO_2-o nanocomposite. The prominent A_1 absorption, which is more common of J-aggregates, also indicates less ordered domains.[87] J-aggregates possess neighbouring P3HT planes that are oriented in a head-to-tail fashion.[87] The irregular and 3D surface of the inverse opal may promote disorder within the P3HT chains which causes the formation of J-aggregates, rather than H-aggregates as seen in the neat P3HT film.

In summary, a series of i-P3HT/TiO_2-o nanocomposites with different periodicities were successfully fabricated. SEM imaging confirmed the inverse opal structure before and after spin coating with P3HT. The photonic properties of the inverse opals were examined via diffuse

reflectance measurements where the stop bands shifted when submerged in water. In addition, diffuse reflectance and absolute absorbance measurements confirmed that the photonic properties of the inverse opal are maintained, despite the high absorption of the P3HT. Photonic properties of the nanocomposites were further confirmed via angle-dependent measurements. Next, the effects of photonic properties on the charge generation of the inverse opals are probed using photoinduced absorption spectroscopy. The relative position of each stop band to the irradiation wavelength and surface area of each inverse opal are explored in the next chapter.

CHAPTER 3

Photoinduced absorption spectroscopy studies

3.1 Introduction to Photoinduced Absorption Spectroscopy

Photoinduced absorption (PIA) spectroscopy is a pump-probe spectroscopic method that can be used to study the kinetics of transient species.[89] PIA spectroscopy has been used to study charge generation and recombination kinetics in photoactive polymers[90,91], organic photovoltaics[38,92,93] as well as dye-sensitized solar cells[94].

In polymer-based organic and hybrid photovoltaics, excitons are produced as a result of photoexcitation of the donor material (i.e. P3HT) where the exciton will dissociate at a donor-acceptor (i.e. TiO_2) interface. The transfer of the electron leaves behind a positive charge on the polymer backbone which induces a localized structural rearrangement on the polymer backbone. This results in the splitting of the HOMO and LUMO energy levels, which form the low energy (LE) and high energy (HE) mid gap energy levels, seen in figure 3.1.

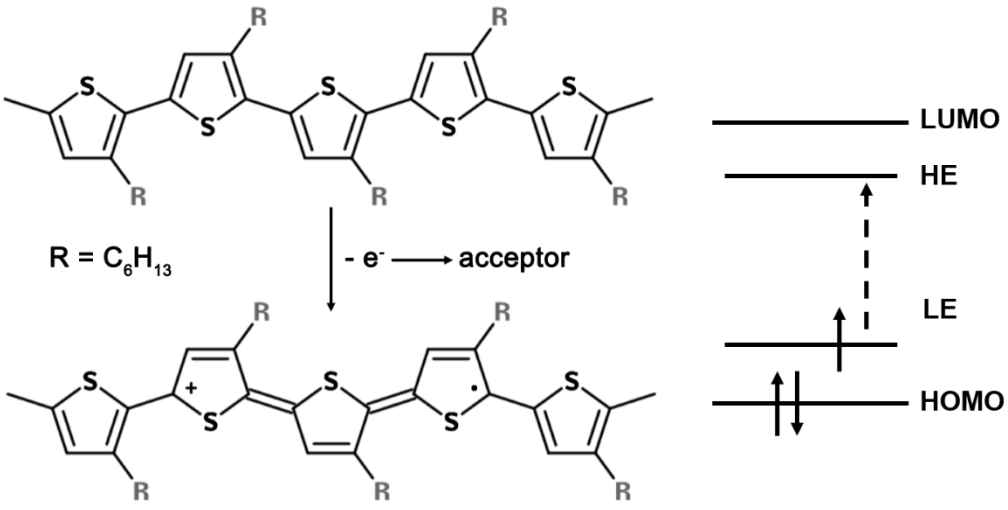

Figure 3.1. Structure of P3HT before and after photoinduced electron transfer which results in the formation of a positive polaron. The corresponding mid-gap LE to HE transition, indicated by the dotted arrow is shown to the left.

Together, the positive charge and structural rearrangement on the backbone is termed a positive polaron. The two new sub-gap energy levels results in three new energy transitions that can be probed. These include the HOMO to LE, LE to HE and HOMO to HE.[95] PIA spectroscopy allows for the detection of the LE to HE transition (~1000 nm) making it a useful technique for probing the charge generation of an active layer.

The quasi steady-state transient spectroscopy uses a square-wave modulated pump beam of narrow bandwidth to excite the polymer. The probe beam is typically a white light source monitored by a detector. A lock-in amplifier, tuned to the frequency of the modulated excitation light source, is used to extract the absorption of the transient species. A lock-in amplifier uses a method known as phase-sensitive detection where the detected signal will be reported with respect to its phase. The lock-in amplifier output is proportioned between two channels, X and Y. The X channel output reports signals that are in-phase with the excitation source, while the Y channel output reports signals that are phase-shifted 90°. In other words, a signal produced by a sample will be seen in one channel or both, depending on its phase. This provides an indication towards the lifetime of the detected signal where short-lived signals will have a greater output in the X channel and long-lived signals will have a greater output in the Y channel. Herein, PIA was employed to study the polaron generation of the i-P3HT/TiO_2-o nanocomposites to address any potential photonic effects. The polaron generation of the i-P3HT/TiO_2-o nanocomposites was compared to reference films of P3HT/PCBM blend and a P3HT/mTiO_2 bilayer. The PIA spectra of the i-P3HT/TiO_2-o series indicated that the magnitude of the LE to HE absorption peak was highly dependent on the stop band position as well as the thickness and quality of the inverse opal.

3.2 Experimental

3.2.1 Photoinduced Absorption Spectroscopy Setup

The i-P3HT/TiO_2-o were mounted in a vacuum-sealed chamber to reduce the degradation of P3HT. A quartz tungsten halogen (QTH) light source (Newport Oriel Apex Monochromator Illuminator 70528) with a 550 nm longpass filter was used as the probe beam and light-emitting diodes (LED) (Luxeon Star Rebel, 700 mA), modulated by a function generator (Tektronix AFG2021), was used as the pump beam. Blue (470 nm) and green (530 nm) LEDs were used in combination with 460 and 525 nm bandpass filters, respectively to excite the nanocomposite at 200 Hz. A silicon/indium gallium arsenide (Si/InGaAs) dual band photodiode (Thorlabs DSD2) was used to detect the monochromated (Princeton Instruments, Acton SP2150) light from the probe beam. Spectra were obtained from 600 to 1700 nm in 10 nm intervals with 60 averages taken at each wavelength. A lock-in amplifier (Stanford Research Systems SR830), in phase with the LED pump light, was used to extract the fractional changes (ΔT) from the probe beam signal, which were reported normalized to probe beam transmission values (T). An outline of the setup is shown in figure 3.2.

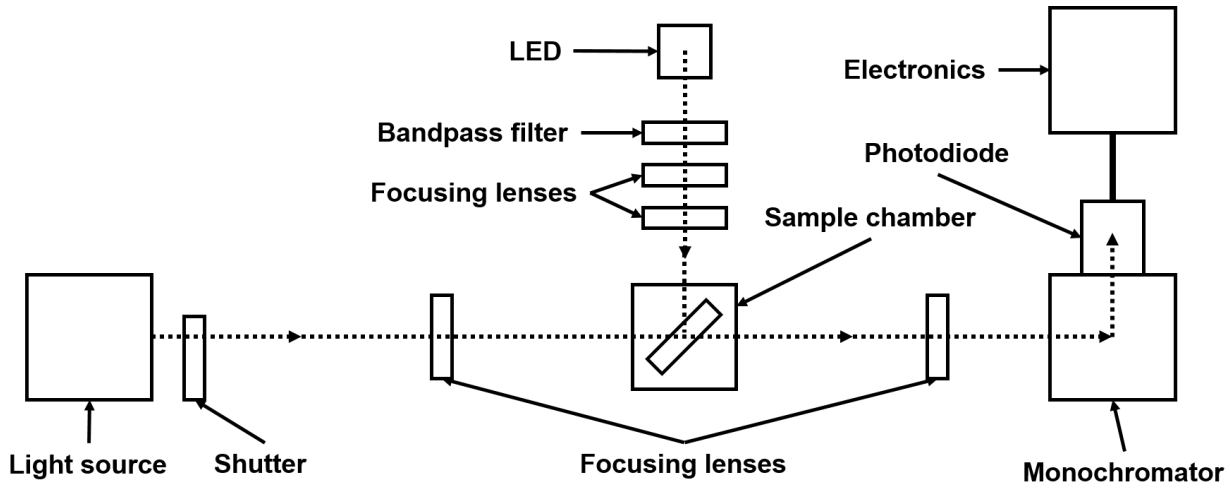

Figure 3.2. Schematic of the PIA setup used in this study. The dotted line represents the path of light of the pump and probe beam.

3.2.2 Pump Modulation Frequency Setup

To perform pump modulation frequency dependence studies, an InGaAs transimpedence amplified detector (Thorlabs, PDA10CS) was used in place of the dual band Si/InGaAs detector. The bandpass filter used in the QTH light source was switched to a 900 nm longpass filter as all spectra were monitored at a fixed of wavelength of 1000 nm. Spectra were taken by modulating the pump beam at different frequencies ranging from 10 to 1000 Hz with 60 averages taken at 30 points.

3.3 Results and Discussion

The photoinduced absorption spectra of all i-P3HT/TiO_2-o nanocomposites revealed two peaks consistent for the entire series. The first broad peak, centered at approximately 760 nm can be assigned as electroabsorption (EA) feature, while the second sharper peak, at 1000 nm, is attributed to the LE to HE transition. In addition, a select few nanocomposites displayed a broad

absorption at wavelengths above 1200 nm, which could possibly be due to the absorption of shallow trapped electrons near the conduction band of TiO_2. As the lock-in amplifier is phase-sensitive, the signal output is split between the X and Y channels with respect to the phase/lifetime of the signal.

Prior to testing i-P3HT/TiO_2-o nanocomposites, the effect of the intensity of the excitation LED on the polaron peak was determined to find a suitable intensity to perform measurements. As expected, the magnitude of the polaron peak increases with increasing LED intensity, shown in figure 3.3.

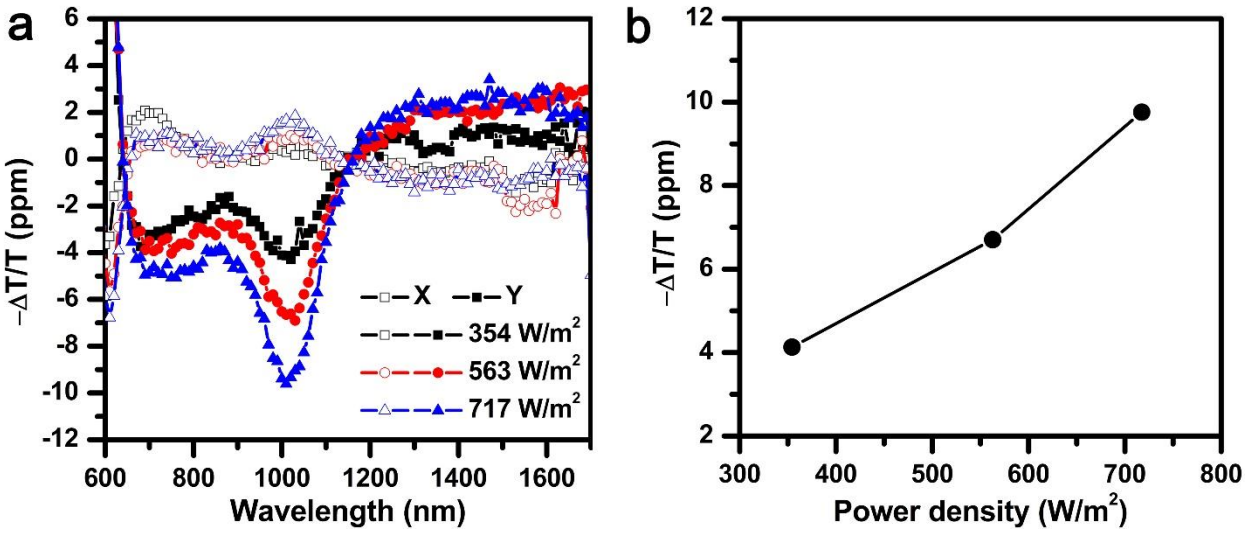

Figure 3.3. PIA spectra of a 440-i-P3HT/TiO_2-o excited under different intensities of blue light (a) and the total PIA signal at 1000 nm as a function of power density of the LED pump beam (b).

All subsequent PIA measurements were carried out at an LED intensity of 563 W/m^2. The linear dependence of charge generation shows no saturation in this range of excitation intensity.

3.3.1 Polaron Transition Probed by PIA

The PIA spectra of the i-P3HT/TiO_2-o nanocomposites were compared to two reference films consisting of a P3HT/PCBM blended film and a P3HT/mTiO_2 bilayer film. Figure 3.4 reveals that the i-P3HT/TiO_2-o nanocomposites consistently produced on average 2 to 3 times greater signal compared to the organic blend and bilayer films.

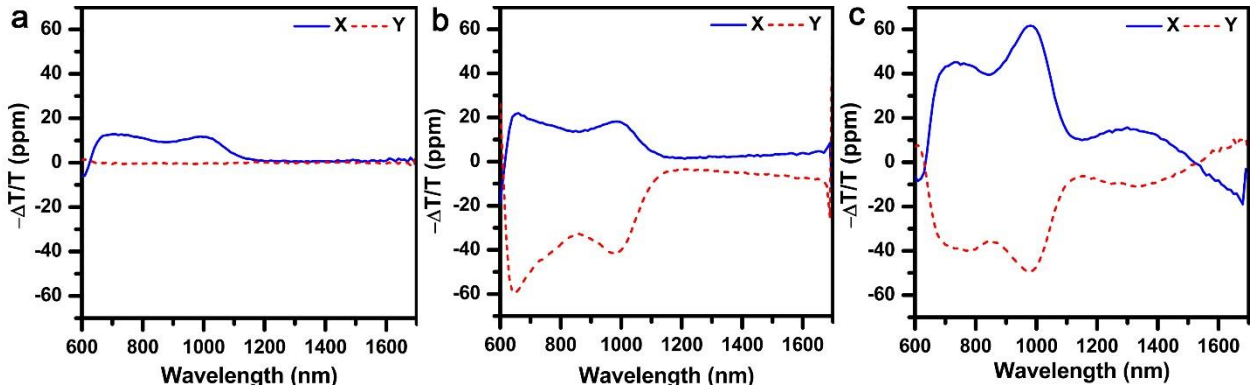

Figure 3.4. PIA spectra comparison of the P3HT/PCBM blend (a), P3HT/mTiO_2 bilayer (b) and i-P3HT/TiO_2-o nanocomposite (c). Solid blue lines represent the in-phase X channel while the dotted red lines represent the out-of-phase Y channel.

The greater polaron generation in the i-P3HT/TiO_2-o is most likely due to the greater interface compared to the blend and bilayer. The macroporous nature of the i-P3HT/TiO_2-o provides a much larger surface area than the bilayer P3HT/mTiO_2 which increases the probability of charge generation. When comparing the bilayer and i-P3HT/TiO_2-o nanocomposites to the P3HT/PCBM blend, a significant proportion of the polaron peak was seen in the phase-shifted Y channel. This indicates that polarons produced in the inorganic hybrids, are longer lived compared to the organic film, which will be discussed in section 3.3.5.

The photoluminescence (PL) spectra of these systems can also provide information regarding the amount of recombination present. PL quenching is often an indicator for the formation of free charge carriers, as the free electron is transferred into the acceptor and is unable to decay radiatively in the donor (P3HT) phase.[96] The PL spectra obtained for a P3HT film, i-P3HT/TiO_2-o, P3HT/mTiO_2 and P3HT/PCBM are shown in figure 3.5.

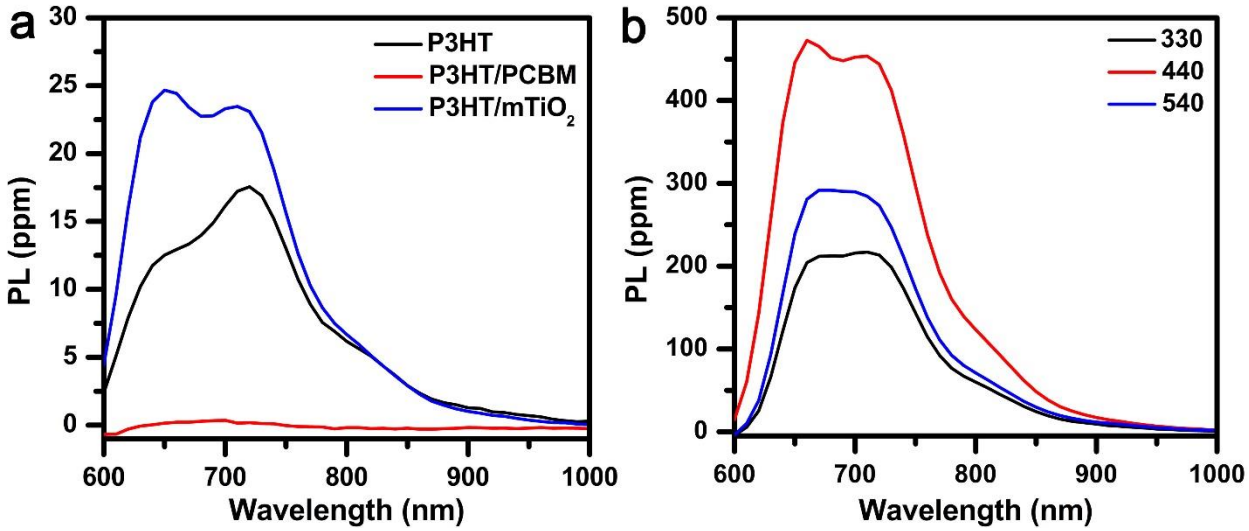

Figure 3.5. PL spectra of reference films (a) and select i-P3HT/TiO_2-o nanocomposites (b). Spectra are collected under blue excitation.

Figure 3.5a suggests that a majority of the excitons produced in the P3HT/PCBM blend are separated into free charge carriers, as shown by the lack of any PL peak. The inorganic hybrids, however, show different degrees of PL. The P3HT/mTiO_2 bilayer film (Fig. 3.5a) displays some PL indicating that there is some radiative decay in this system, comparable to that of the pristine P3HT film. In comparison, the i-P3HT/TiO_2-o nanocomposites display an order of magnitude greater PL signal. Despite this, the i-P3HT/TiO_2-o nanocomposites consistently produced greater polaron signals with respect to the two reference films. This observation

indicates that a greater number of excitons are produced in the i-P3HT/TiO_2-os relative to the two reference films, but a significant proportion of the excitons produced are not dissociated and thus results in a large PL signal. Some P3HT in i-P3HT/TiO_2-o might not be in direct contact with TiO_2 and hence exhibit PL.

3.3.2 Electroabsorption Feature

The electroabsorption (EA) peak seen at wavelengths below 750 nm is due to the Stark effect. The Stark effect arises upon the dissociation of an exciton into an electron-hole pair. The separated electron-hole pair produces an electric field which alters the energy levels in the polymer.[97] The electric field shifts the absorption profile of the polymer and the difference between the ground and excited state absorption spectra results in the EA feature.[98] This EA feature is consistent with previous findings for P3HT donor-acceptor systems.[37,99–103] The PIA spectra of P3HT/PCBM and P3HT/mTiO_2 films also display the EA peak, where it was consistently more prominent than the polaron peak at 1000 nm. In contrast, the EA peak of the i-P3HT/TiO_2-os is more suppressed. The smaller EA feature in the inverse opals may be due to the higher effective dielectric constant of the organic/inorganic hybrid. The higher dielectric constant of the inorganic acceptor (TiO_2) screens the localized electric field generated from the long range Coulombic attraction of charge carriers more effectively than an organic acceptor (i.e. PCBM), thereby reducing the magnitude of the electro-absorption feature.[98] Although the P3HT/mTiO_2 and i-P3HT/TiO_2-o both have a higher effective dielectric constants, the i-P3HT/TiO_2-o had a lower EA feature with respect to the polaron peak. The lower EA feature indicates that the charges are more effectively screened in the i-P3HT/TiO_2-o than the

P3HT/mTiO$_2$. The greater degree of screening may be attributed to the number of traps, as the inverse opal has a much larger surface in comparison to the P3HT/mTiO$_2$ bilayer.

3.3.3 Infrared Absorption

Figure 3.6 shows the PIA spectra of select i-P3HT/TiO$_2$-o nanocomposites that exhibit absorption at wavelengths above 1100 nm. The assignment of the infrared absorption is difficult as the absorptions are either featureless or broad, or are not centered at a certain wavelength.

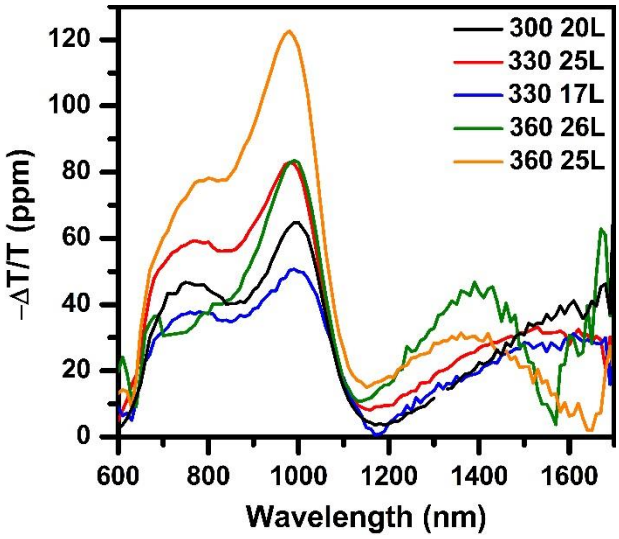

Figure 3.6. PIA spectra of select i-P3HT/TiO$_2$-o nanocomposites displaying the near-IR (>1200 nm) absorption feature. The number of layers for each nanocomposite is listed after the label in the legend.

Previous research has identified the presence of three reactive species in photoexcited nanocrystalline TiO$_2$ films: trapped holes, free electrons and trapped electrons.[104] The absorption spectra of these reactive species are sensitive to the nature of the trap, where the shape and position of the peak can indicate the depth of the trap. Several studies have observed a continually increasing absorption with respect to wavelength and was attributed to the intra-band

transition of free electrons in the conduction band.[104–106] The free electrons could be the origin for some of the broad featureless IR absorption. Another source for absorption in the IR region is due to the direct optical transition from a trap state to the conduction band.[107] This absorption is characterized by a broad peak appearing at approximately 1100 nm. Theoretical studies have identified the different types of defect states in reduced TiO_2. Two of the defect states have been calculated placing the energy levels at 0.8 eV and 0.7 eV below the conduction band.[108] The high surface area of the TiO_2 inverse opal could give rise to large population of defect states, though the origin of IR absorption in our data could not be assigned to those found in the literature.

3.3.4 Probing Photonic Effects on Polaron Generation

Figure 3.7 shows the PIA spectra of the 300-, 400- and 440-i-P3HT/TiO_2-o under blue and green excitation. Using different excitation light sources allows the investigation of photonic effects on polaron generation; in the absence of any photonic properties, the i-P3HT/TiO_2-o would behave similarly. Under blue excitation, the 400-i-P3HT/TiO_2-o produced the greatest overall polaron generation; however under green light it does not. In contrast, the 440-i-P3HT/TiO_2-o produced the greatest polaron under green light but not under blue light. This observation indicates possible photonic enhancements in i-P3HT/TiO_2-o nanocomposites. Table 3.1 summarizes the magnitude of polaron signal for this set of i-P3HT/TiO_2-o.

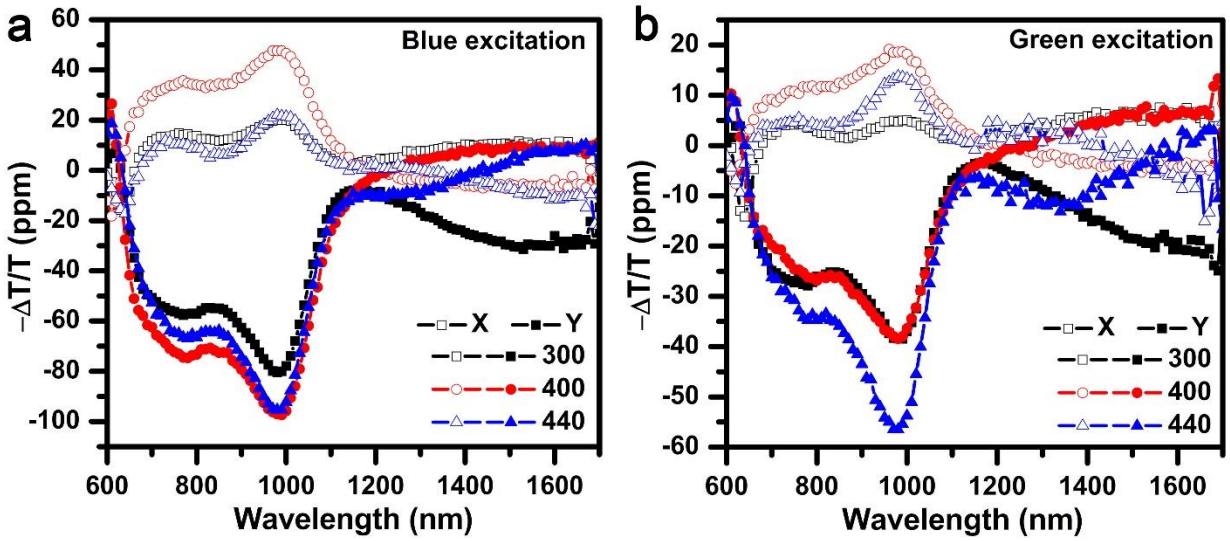

Figure 3.7. PIA spectra of 300- (squares), 400- (circles) and 440-i-P3HT/TiO_2-o (triangles) excited under blue (470 nm) (a) and green (530 nm) (b) light. X channels are indicated by open symbols and Y channels are shown as solid symbols.

Table 3.1. Summary of the total polaron signal obtained for each nanocomposite in Fig. 3.8 under blue and green excitation. The total polaron signal, R, is calculated by $R = \sqrt{X^2 + Y^2}$.

Nanocomposite	**Total polaron signal, -ΔT/T (ppm)**	
	Blue excitation (470 nm)	**Green excitation (530 nm)**
300-i-P3HT/TiO_2-o	82	39
400-i-P3HT/TiO_2-o	108	42
440-i-P3HT/TiO_2-o	98	57

To investigate the photonic enhancement in detail, PIA spectra were obtained for multiple samples of each i-P3HT/TiO_2-o in the complete series under blue (470 nm) and green (530 nm) excitation. To determine the presence of photonic effects, all other variables must be taken into consideration, the main factors being the amount of P3HT present on each inverse

opal and the total available surface area of each inverse opal. Figures 3.8a and 3.9a show the average polaron signals for each i-P3HT/TiO_2-o under blue and green excitation, respectively. Figure 3.8b and 3.9b show the reflectance spectra of the corresponding i-P3HT/TiO_2-o with the excitation region shaded for reference.

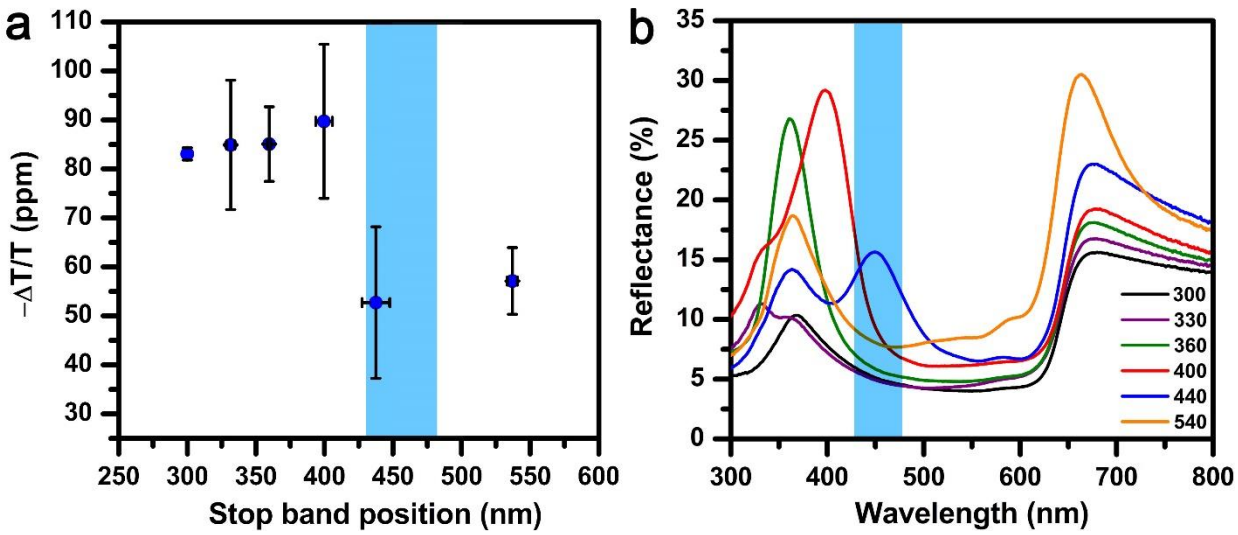

Figure 3.8. Polaron generation at 1000 nm with respect to the stop band position of i-P3HT/TiO_2-o under blue excitation (a) with the corresponding reflectance spectra of the i-P3HT/TiO_2-o (b). -ΔT/T values reported are averages of at least three samples and are normalized to the amount of P3HT present on each nanocomposite. Shaded areas represent the excitation wavelength range. A total of 37 samples were tested with standard error of the mean reported.

Note that the polaron signals are normalized with respect to the amount of P3HT on each nanocomposite, thus accounting for any variations in the amount of P3HT. The quantification of P3HT was carried out by dissolving P3HT from the nanocomposites in toluene upon completion of the PIA experiments. The absorbance of the P3HT solutions were taken and indicated that all

i-P3HT/TiO_2-os had a comparable amount of P3HT (table 3.2) despite the change in periodicity from 140 to 375 nm.

Table 3.2. Average absorbance data of P3HT solutions dissolved from the inverse opals.

Nanocomposite	Number of samples	Average absorbance	Standard error of the mean
300-i-P3HT/TiO_2-o	4	0.730	0.070
330- i-P3HT/TiO_2-o	9	0.705	0.038
360- i-P3HT/TiO_2-o	10	0.765	0.033
400- i-P3HT/TiO_2-o	6	0.773	0.052
440- i-P3HT/TiO_2-o	4	0.776	0.116
540- i-P3HT/TiO_2-o	6	0.644	0.056

For the purpose of this research, the 300-i-P3HT/TiO_2-o acts as a reference, where the stop band is sufficiently far enough from the excitation wavelengths preventing any possible enhancement. Under blue excitation (Fig. 3.8a), an increase in polaron generation is observed when the stop band changes from 300 nm to 330, 360 and 400 nm, with the 400-i-P3HT/TiO_2-o displaying the greatest amount of polaron generation. These inverse opals have stop bands centered to the left of the excitation wavelength region. The slow photon enhancement seen for photonic crystals occurs on the red edge of the photonic stop band, where the interaction between light and the high refractive index material (TiO_2) is maximized.[74] Less photonic enhancement will be observed as the slow photon region moves farther from excitation region. The photonic effect of the 440-i-P3HT/TiO_2-o can also be observed. The 440-i-P3HT/TiO_2-o exhibits a significant decrease in the polaron signal, which is due to the stop band being centered within the

excitation region. As some light is reflected, the light interaction with the nanocomposite is reduced resulting in a decrease in the number of polarons generated.

Under green excitation, an overall exponential-like decrease in polaron generation was observed with increasing stop band position. The 300-, 360- and 330-i-P3HT/TiO_2-o have stop bands relatively far from the excitation wavelength region (Fig. 3.9a) while the 540-i-P3HT/TiO_2-o has a suppressed stop band centered close to the excitation wavelength. The 540-i-P3HT/TiO_2-o exhibits some reflectivity within the absorption range of P3HT (400 – 550 nm) and exhibits the lowest amount of polaron generation. The 400-i-P3HT/TiO_2-o and 440-i-P3HT/TiO_2-os have stop bands with the red edge closer to the excitation wavelength and are most likely to experience a photonic enhancement. A slight increase in polaron generation is seen for these two nanocomposites compared to 360-i-P3HT/TiO_2-o, however the increase is almost negligible. It is plausible that the relative surface area of inverse opals counteracts the photonic enhancements.

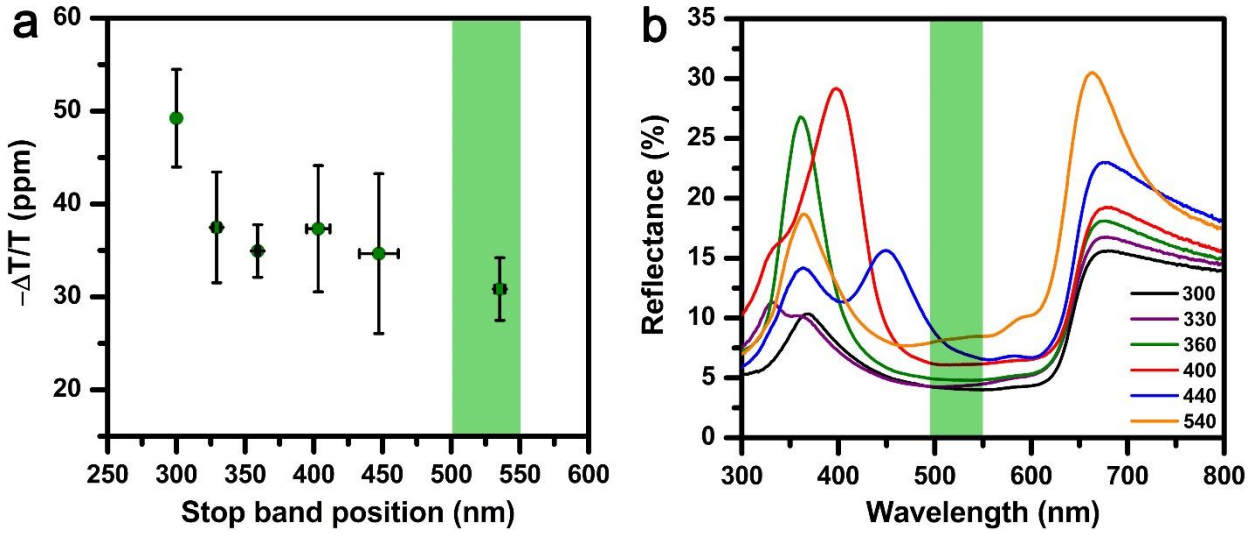

Figure 3.9. Polaron generation at 1000 nm with respect to the stop band for each i-P3HT/TiO_2-o under green excitation (a) with the corresponding reflectance spectra of the i-P3HT/TiO_2-o (b). -ΔT/T values reported are averages of at least three samples and are normalized to the amount of P3HT present on each nanocomposite. Shaded areas represent the excitation wavelength range. A total of 36 samples were tested with standard error of the mean reported.

The amount of surface area for a given volume, is inversely proportional to the periodicity of the inverse opal. A smaller surface area will result in less interface with the P3HT, which will decrease the number of polarons generated. The area for each inverse opal can be calculated by determining the total area of the number of spheres for a given volume. This relation is proportional to 1/r, where r represents the radius of the sphere. Figure 3.10 shows a plot of the relative surface area with respect to the stop band position of the inverse opal. Table 3.3 outlines the calculated areas of each inverse opal for a specific volume.

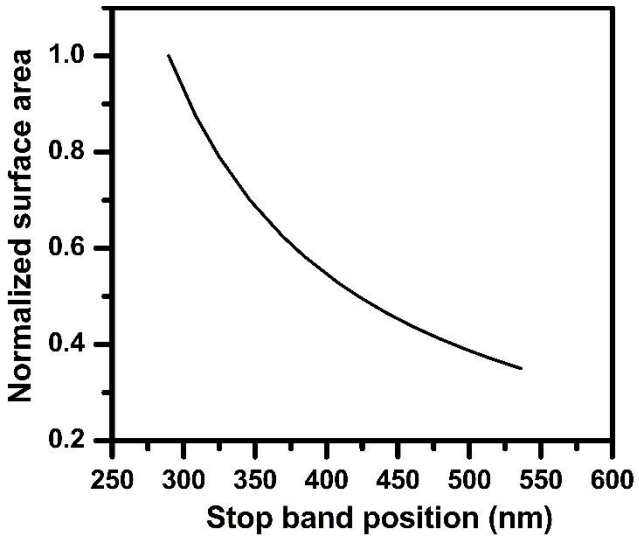

Figure 3.10. Surface area of an inverse opal normalized to the surface area of the 300-i-TiO_2-o with respect to the stop band position.

Table 3.3. Surface area of inverse opals with respect to the diameter of sphere in the opal template.

Diameter of sphere (nm)	**Corresponding Nanocomposite**	**Surface area (mm^2) of a 1 cm x 1 cm x 1000 nm inverse opal**	**Normalized surface area**
140	300- i-P3HT/TiO_2-o	3173	1.000
177	330- i-P3HT/TiO_2-o	2510	0.791
224	360- i-P3HT/TiO_2-o	1983	0.625
265	400- i-P3HT/TiO_2-o	1676	0.528
320	440- i-P3HT/TiO_2-o	1388	0.438
375	540- i-P3HT/TiO_2-o	1184	0.373

Figure 3.10 reveals a significant decrease in surface area as the periodicity increases from the 300-i-TiO_2-o to the 330-i-TiO_2-o, with each subsequent inverse opal displaying a reduction in area. Neglecting any photonic enhancements, an inverse opal with a large surface area should

produce a greater amount of charge in comparison to an inverse opal with a reduced surface area. This factor may contribute to the trend seen in figure 3.9a. It also suggests that the photonic enhancement for 330-, 360- and 400- i-P3HT/TiO_2-os under blue excitation (Fig. 3.8a) may be more prominent if the decrease in interface was taken into account.

Based on the PIA spectra for the nanocomposite series under blue and green light, certain sizes of i-P3HT/TiO_2-o displayed enhanced polaron generation. The amount of polaron generation decreases as the periodicity of the inverse opal increased. This was attributed to the reduced interface in the inverse opals with larger periodicities. Despite this, the 330-, 360-, and 400-i-P3HT/TiO_2-o nanocomposites displayed enhanced polaron generation under blue excitation. This was due to the excitation region being within the slow photon region enhancing the light-matter interaction. In contrast, the 440-i-P3HT/TiO_2-o displayed a reduced polaron generation as its stop band was aligned within the excitation region, reflecting some of the light. Under green light, a slight photonic enhancement was seen for the 400- and 440-i-P3HT/TiO_2-o while the 540-i-P3HT/TiO_2-o produced the least number of polarons, most likely due to the combined effects of the reflectance from the stop band and reduced interface.

3.3.5 Polaron Lifetime Measurements

Pump modulation dependence studies were performed to determine the lifetime of the polarons. The polaron signal depends on the pump modulation frequency: polarons that possess lifetimes longer than the inverse of the pump modulation frequency will not be able to decay within the pump's duty cycle. Long-lived polarons will therefore have a faster falloff as the frequency increases which is also indicative of a broad distribution of polaron lifetimes.[37]

Figure 3.11 shows the lifetime measurements of the i-P3HT/TiO_2-o in comparison to the two reference films, P3HT/PCBM and P3HT/mTiO_2. The inorganic hybrids consistently produced polaron signals that were more sensitive to changes in frequency than the P3HT/PCBM blend, indicating that the inorganic hybrids have longer lived polarons.

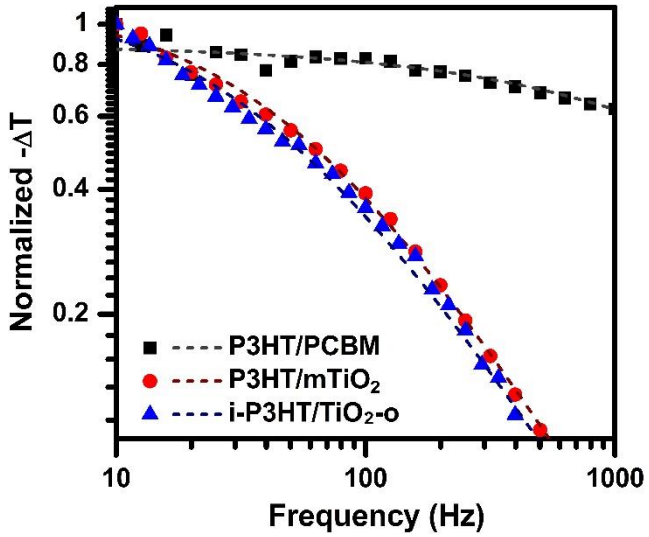

Figure 3.11. Polaron lifetime measurements of a P3HT/PCBM film (black squares), a P3HT/mTiO_2 bilayer (red circles) and a i-P3HT/TiO_2-o nanocomposite (blue triangles). The dotted lines show the dispersive recombination fitting for each respective film. A faster falloff is observed for the inorganic hybrids indicating longer lived polarons.

A dispersive recombination model was used to obtain an average lifetime for the each sample. This model accounts for trap states which are more common in hybrid donor-acceptor systems. The equation is as follows:

$$-\frac{\Delta T}{T} = \frac{\left(\frac{\Delta T}{T}\right)_0}{1+(\omega\tau)^\gamma} \qquad 1.5$$

where $(\Delta T/T)_0$ is the PIA signal at 0 Hz, ω is the pump modulation frequency, τ is the average lifetime and γ describes the dispersity of polaron lifetimes, where values are equal to or less than 1 with values closer to 1 indicating less dispersity.[99] Average lifetimes for the polarons in i-P3HT/TiO_2-o nanocomposites were comparable to other inorganic systems. Inorganic hybrid systems using conjugated polymer with CdSe quantum dots, nanoporous ZnO and TiO_2 films produced lifetimes ranging from 3 – 13 ms, 2 ms and 2 – 12 ms, respectively.[37,43,99] On average, the lifetimes of the P3HT/mTiO_2 bilayers and i-P3HT/TiO_2-os were 35 ± 10 ms and 29 ± 4 ms, respectively, while lifetimes for the P3HT/PCBM films resulted in lifetimes of approximately 0.26 ± 0.01 ms. The longer lifetimes observed from the hybrids may be due to the screening of long-range Coulombic interactions due to the higher dielectric constant of TiO_2 and/or the abundance of traps due to surface defects.[99] The reduced EA feature in inorganic hybrids, compared to that of the P3HT/PCBM blend, indicates that the larger dielectric constant plays a role in mitigating the internal electric field produced by the long range interaction between charge carriers. As a result, the greater dielectric constant of TiO_2 would also increase polaron lifetimes by hindering recombination rates. The nanostructured inverse opal also has a large surface area which would increase the population of surface traps. Charge carriers caught in surface traps could reduce carrier mobilities and slow down recombination.[99]

The PIA spectra of the i-P3HT/TiO_2-o displayed varied proportions of X and Y signals and was therefore assumed to be directly related to the lifetime of the polarons. Figure 3.12 shows a plot of the lifetime of the polarons with respect to the proportion of Y to X signals at 1000 nm (polaron peak).

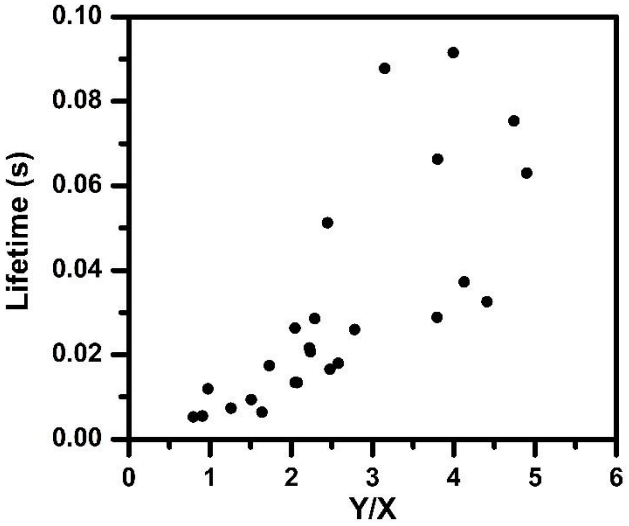

Figure 3.12. Polaron lifetimes with respect to the proportion of Y to X signal at 1000 nm. Lifetimes are shown for a majority of i-P3HT/TiO_2-o that were excited by blue light.

Inverse opal nanocomposites with a greater proportion of polaron signal in the Y channel are observed to possess longer lifetimes. This is due to the 90° phase-shift of the Y channel which displays delayed signals with the magnitude of the signal being directly related to the lifetime.

3.3.6 Inverse Opal Thickness Effects

Previous studies using reflectance, transmission and white light interferometry measurements in combination with theoretical measurements have been done to determine the effect of thickness on the photonic properties of the opals. An increase in the thickness of the opal results in a decrease in the width of the stop band and an increase in the intensity of the stop band reflection, up to approximately 30 layers.[81] The slow photon enhancement seen at the edges of the stop band would be directly affected. In addition, the group velocity of photons at the band edges have also been shown to decrease with increased sample thickness.[79] A thicker

opal, however, is accompanied by more imperfections which causes the scattering of light to counteract the effect of the reduced group velocity.[79]

To investigate the effects of inverse opal thickness, i-P3HT/TiO_2-os were made using two inverse opal sizes, 330-i-TiO_2-o and 360-i-TiO_2-o, each with varying thicknesses and excited under blue and green light. The 330-i-P3HT/TiO_2-o acts as a control since the stop band is too far from the excitation wavelengths to experience any photonic enhancement, whereas the 360-i-P3HT/TiO_2-o is close enough under blue excitation to take advantage of the slow photon enhancement. Measurements of the i-P3HT/TiO_2-o have shown that the thicknesses directly affected the amount of polarons generated for each respective nanocomposite. Approximately 18 nanocomposites were tested for each inverse opal size and thicknesses ranged from 13 to 29 layers for the 330-i-P3HT/TiO_2-os while thicknesses for the 360-i-P3HT/TiO_2-o ranged from 10 – 25 layers (Fig. 3.13).

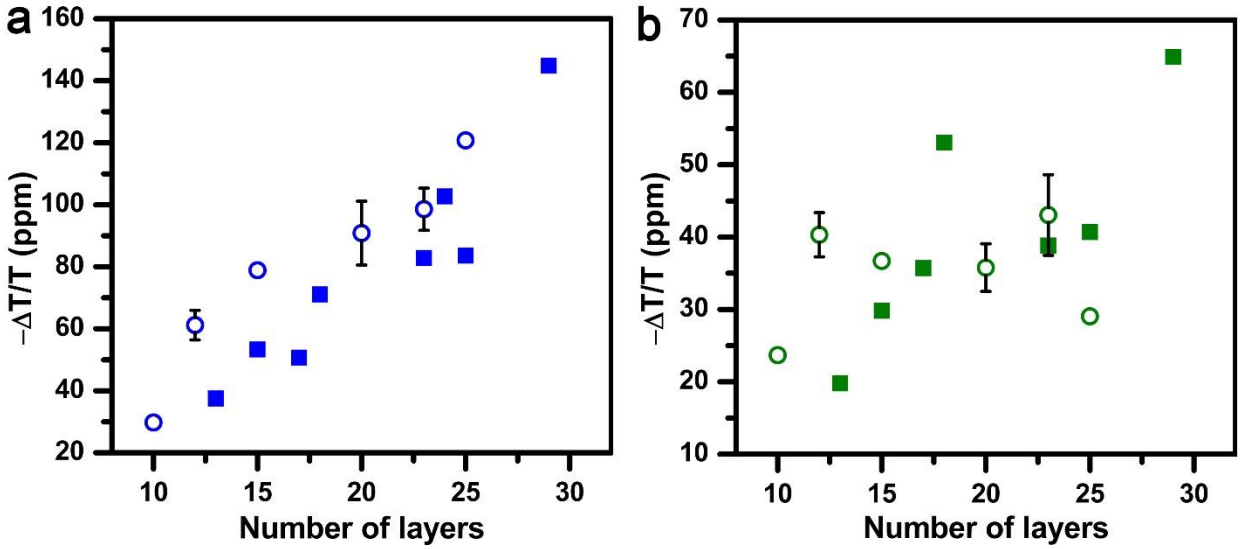

Figure 3.13. Dependence of polaron generation on the number of layers for 330-i-P3HT/TiO_2-o (solid squares) and 360-i-P3HT/TiO_2-o (open circles) nanocomposites under blue (a) and green excitation (b).

Under blue excitation, it was expected that the 360-i-P3HT/TiO_2-o would produce a greater amount of polaron generation per layer than the 330-i-P3HT/TiO_2-o, since the red edge of the 360-i-P3HT/TiO_2-o is closer to the excitation wavelength. From the obtained results, it was determined that doubling the number of layers, produced approximately a 3 and 2.6 times increase in polaron generation for the 360- and 330-i-P3HT/TiO_2-o nanocomposites, respectively (Fig. 3.13a). The results are similar for both inverse opals which do not support the hypothesis that photonic enhancement would be more pronounced with increasing thickness. However, it should be noted that the 330-i-TiO_2-o has a greater surface area in comparison to the 360-i-TiO_2-o which may counteract any photonic enhancement arising from slow photons.

Under green excitation, the polaron generation was approximately proportional to the number of layers present, where doubling the number of layers would double the amount of polaron generation (Fig. 3.13b). The behaviour of the two inverse opals were comparable, as both stop bands are too far from the excitation region to experience any slow photon enhancement.

The data obtained under blue light demonstrate that the thickness of the inverse opal is directly proportional to the number of polarons generated. An enhancement in polaron generation due to the photonic effects of 360-i-P3HT/TiO_2-o was expected, but not observed. This is most likely due to the reduced surface area offsetting any photonic enhancement. The data obtained under green light, did not provide any conclusive evidence towards the dependence of photonic enhancement on the thickness of the inverse opal. Further testing of more samples and inverse opals with different periodicities is needed to determine any relation between inverse opal thickness and photonic effects.

3.3.7 Device Fabrication and Preliminary Measurements

Preliminary attempts on device fabrication and characterization were carried out. Devices were fabricated from i-P3HT/TiO_2-o nanocomposites to investigate photonic effects on the incident photon to electron conversion efficiency. If the photonic enhancement on charge generation carried over to the device efficiency, one would expect to observe a relative increase in the quantum efficiency spectrum in the slow photon region of the inverse opal. Figure 3.14 shows a schematic of the inverted geometry used to fabricate i-P3HT/TiO_2 devices.

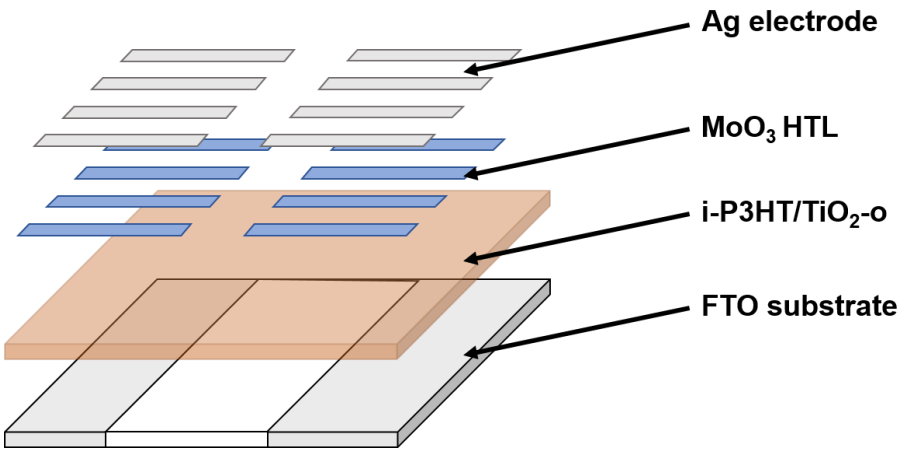

Figure 3.14. Schematic of the i-P3HT/TiO_2 device used for preliminary measurements. An inverted geometry was used with Ag electrodes and a molybdenum oxide (MoO_3) hole transport layer (HTL).

To fabricate devices, 360-i-TiO_2-os were deposited onto etched fluorine-doped tin oxide (FTO) coated substrates. The middle of the substrate was masked off and etched using zinc powder and 1 M hydrochloric acid to remove the conductive coating. The opal template deposition and infiltration conditions were optimized to obtain high quality 360-i-TiO_2-o with layers ranging from 20 to 22 layers. Inverse opals were spin coated with P3HT, under nitrogen atmosphere, to complete the active layer. In addition to the i-P3HT/TiO_2-o device, reference

P3HT/mTiO_2 devices were made for comparison. A mask with an eight finger configuration was put onto the nanocomposites prior to the thermal evaporation of the hole-transport layer (molybdenum oxide, 10 nm) and electrode (silver, 80 nm). The mask resulted in the formation of eight devices per nanocomposite with an approximate area of 2 mm^2 as shown in figure 3.15. The opposite end of the fingers were painted with silver paint to provide a contact point to obtain measurements.

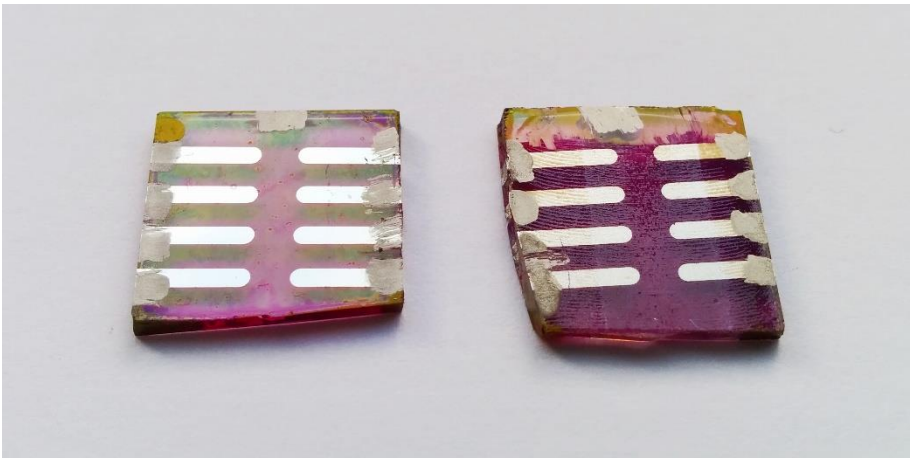

Figure 3.15. Image of a reference P3HT/mTiO_2 (left) and a 360-i-P3HT/TiO_2-o (right) used for device testing. The eight devices are located in the middle of each nanocomposite at the end of each finger.

Current-voltage curves for each device were obtained under simulated AM 1.5G conditions. Preliminary measurements indicated that the devices were short-circuited. Further optimization of the fabrication process and measurement configuration is needed to prevent short-circuits, in order to obtain accurate power conversion efficiencies.

CHAPTER 4

Conclusions and future work

In conclusion, a series of TiO_2 inverse opals with different periodicities were successfully fabricated and coated with P3HT to complete the nanocomposite for the BHJ active layer. Inverse opals were fabricated using high quality self-assembled polystyrene opal templates of different sphere sizes ranging from 140 nm to 375 nm. The opal templates were then infiltrated with $Ti(OBut)_4$ and calcined to yield anatase TiO_2 inverse opals. Structural and optical characterization of the inverse opals were completed using SEM imaging and UV-vis spectroscopy. SEM images confirmed the presence of the periodic and highly ordered fcc structures with varying thicknesses. UV-vis diffuse reflectance measurements were used to determine the stop band positions and confirm the photonic properties of each inverse opal. Upon coating the inverse opals with P3HT to complete the nanocomposite, diffuse reflectance measurements were taken again to ensure the preservation of the photonic properties. Stop bands were observed at approximately the same position with reduced intensity due to the absorbance of the P3HT. The stop band of the 540-i-P3HT/TiO_2-o exhibited the greatest suppression as it was centered within the max absorption of P3HT, but resulted in increased reflectance within this region. Absolute absorbance measurements of the i-P3HT/TiO_2-o nanocomposites were also affected by the presence of the stop band and was characterized by a dip in the absorption. The 400-i-P3HT/TiO_2-o exhibited a slight enhancement in absorption towards the red edge of the stop band, due to the excitation region aligning with the slow photon region. The absorption spectra of the i-P3HT/TiO_2-o nanocomposites also indicate that some disorder may be present due to the irregular surface of the inverse opal.

PIA measurements were obtained for the series of i-P3HT/TiO_2-o nanocomposites under blue and green excitation to elucidate any charge generation enhancement due to the photonic effects of the inverse opal. Polaron generation was expected to decrease with increasing inverse opal periodicity, due to the reduced interface. A photonic enhancement in charge generation was most prominent under blue excitation for the 330-, 360- and 400-i-P3HT/TiO_2-o. Polaron generation increased as the periodicity increased up to the 400-i-P3HT/TiO_2-o, despite the smaller surface area. This was due to the red-shift of the stop band, which moves the slow photon region closer to the excitation region. In addition, the stop band of the 440-i-P3HT/TiO_2-o was aligned within the excitation region and resulted in the reflection of the incident light resulting in decreased polaron generation. The data obtained under green excitation displayed a slight enhancement in polaron generation for the 400- and 440-i-P3HT/TiO_2-o owing to the slow photon enhancement. The 540-i-P3HT/TiO_2-o exhibited the least polaron generation due the combined effects of the reduced interface and the reflectivity of the stop band.

Lifetime measurements for the i-P3HT/TiO_2-o and P3HT/mTiO_2 nanocomposites were observed to be significantly longer than the the P3HT/PCBM blend. The longer lifetimes were attributed to the higher dielectric constant of the TiO_2 resulting in the screening of long-range Coulombic interactions. This was also evident from the PIA spectra where the EA feature for the inorganic hybrids were lower in magnitude with respect to the organic blend.

The thicknesses of the inverse opals were also explored to determine if thicker inverse opals would translate to increased photonic effects. Varying thicknesses of 330- and 360-i-TiO_2-o were fabricated and coated with P3HT which were then tested under blue and green light. It was expected that the 360-i-P3HT/TiO_2-o would exhibit stronger photonic effects as its stop band is closer to the blue excitation region; however a similar increase in polaron generation

with respect to increasing thickness was observed for both nanocomposites. Further testing of more samples and inverse opals with different periodicities are needed in order to make any conclusions regarding the dependence of photonic properties on the thickness of the inverse opals.

Future goals for this research include the fabrication of devices using i-P3HT/TiO_2-o nanocomposites to elucidate the photonic effects on device efficiencies. The fabrication of devices will need to be optimized to ensure accurate measurement can be obtained. In addition, the surface passivation of traps on the TiO_2 inverse opal are an interesting research route, as the reduction of traps may play a role in altering the photonic effects and polaron generation of i-P3HT/TiO_2-o nanocomposites.

The successful integration of TiO_2 inverse opals into the active layer of a BHJ system and the indications of slow photon enhancement has provided considerable insight towards the use of photonic crystals for optically-enhanced solar cells. The highly ordered and large interfacial area between the inverse opal and P3HT has a significant influence on the number of polarons generated by the hybrid active layer. In addition, the photonic effects of the inverse opal were most pronounced at wavelengths with low absorption. The interfacial area and photonic properties in low absorbing materials may prove to be useful for designing the morphology of active layer and enhancing absorption. The research presented in this thesis serves as a proof-of-concept, where the photonic and structural properties of the inverse opals can be applied to other systems to enhance light-matter interactions.

REFERENCES

(1) Darling, S. B.; You, F. The Case for Organic Photovoltaics. *RSC Adv.* **2013**, *3* (39), 17633.

(2) Dennler, G.; Scharber, M. C.; Brabec, C. J. Polymer-Fullerene Bulk-Heterojunction Solar Cells. *Adv. Mater.* **2009**, *21* (13), 1323–1338.

(3) Global Energy Statistical Yearbook 2015 https://yearbook.enerdata.net/.

(4) U.S. Energy Information Administration. *Levelized Cost and Levelized Avoided Cost of New Generation Resources in the Annual Energy Outlook 2014*; 2015.

(5) U.S. Energy Information Administration. *Short-Term Energy Outlook*; 2016.

(6) U.S. Energy Information Administration. *International Energy Outlook 2014*; 2014.

(7) Shafiee, S.; Topal, E. When Will Fossil Fuel Reserves Be Diminished? *Energy Policy* **2009**, *37* (1), 181–189.

(8) U.S. Energy Information Administration. *Annual Energy Outlook 2015*; 2015.

(9) IRENA. *Renewable Energy Technologies: Cost Analysis Series - Solar Photovoltaics*; Vol. 1.

(10) Best Research-Cell Efficiencies http://www.nrel.gov/ncpv/images/efficiency_chart.jpg.

(11) Scharber, M. C.; Sariciftci, N. S. Efficiency of Bulk-Heterojunction Organic Solar Cells. *Prog. Polym. Sci.* **2013**, *38* (12), 1929–1940.

(12) Green, M. A.; Emery, K.; Hishikawa, Y.; Warta, W.; Dunlop, E. D. Solar Cell Efficiency Tables (Version 45). *Prog. Photovoltaics Res. Appl.* **2015**, *23* (1), 1–9.

(13) Søndergaard, R.; Hösel, M.; Angmo, D.; Larsen-Olsen, T. T.; Krebs, F. C. Roll-to-Roll Fabrication of Polymer Solar Cells. *Mater. Today* **2012**, *15* (1-2), 36–49.

(14) Dang, M. T.; Hirsch, L.; Wantz, G. P3HT:PCBM, Best Seller in Polymer Photovoltaic Research. *Adv. Mater.* **2011**, *23* (31), 3597–3602.

(15) Scharber, M. C.; Mühlbacher, D.; Koppe, M.; Denk, P.; Waldauf, C.; Heeger, A. J.; Brabec, C. J. Design Rules for Donors in Bulk-Heterojunction Solar Cells—Towards 10 % Energy-Conversion Efficiency. *Adv. Mater.* **2006**, *18* (6), 789–794.

(16) Armaroli, N.; Balzani, V. The Future of Energy Supply: Challenges and Opportunities. *Angew. Chemie Int. Ed.* **2007**, *46* (1-2), 52–66.

(17) Krebs, F. C.; Nielsen, T. D.; Fyenbo, J.; Wadstrøm, M.; Pedersen, M. S. Manufacture, Integration and Demonstration of Polymer Solar Cells in a Lamp for the "Lighting Africa" Initiative. *Energy Environ. Sci.* **2010**, *3* (5), 512.

(18) Azzopardi, B.; Emmott, C. J. M.; Urbina, A.; Krebs, F. C.; Mutale, J.; Nelson, J. Economic Assessment of Solar Electricity Production from Organic-Based Photovoltaic Modules in a Domestic Environment. *Energy Environ. Sci.* **2011**, *4* (10), 3741.

(19) Narasimhan, V. K.; Cui, Y. Nanostructures for Photon Management in Solar Cells. *Nanophotonics* **2013**, *2* (3), 1–24.

(20) He, Y.; Chen, H. Y.; Hou, J.; Li, Y. Indene - C60 Bisadduct: A New Acceptor for High-Performance Polymer Solar Cells. *J. Am. Chem. Soc.* **2010**, *132* (4), 1377–1382.

(21) Liang, Y.; Xu, Z.; Xia, J.; Tsai, S. T.; Wu, Y.; Li, G.; Ray, C.; Yu, L. For the Bright Future-Bulk Heterojunction Polymer Solar Cells with Power Conversion Efficiency of 7.4%. *Adv. Mater.* **2010**, *22* (20), 135–138.

(22) Dou, L.; Gao, J.; Richard, E.; You, J.; Chen, C.-C.; Cha, K. C.; He, Y.; Li, G.; Yang, Y. Systematic Investigation of Benzodithiophene- and Diketopyrrolopyrrole-Based Low-Bandgap Polymers Designed for Single Junction and Tandem Polymer Solar Cells. *J. Am. Chem. Soc.* **2012**, *134* (24), 10071–10079.

(23) You, J.; Dou, L.; Yoshimura, K.; Kato, T.; Ohya, K.; Moriarty, T.; Emery, K.; Chen, C.-C.; Gao, J.; Li, G.; Yang, Y. A Polymer Tandem Solar Cell with 10.6% Power Conversion Efficiency. *Nat. Commun.* **2013**, *4*, 1446.

(24) Roncali, J.; Leriche, P.; Blanchard, P. Molecular Materials for Organic Photovoltaics: Small Is Beautiful. *Adv. Mater.* **2014**, *26* (23), 3821–3838.

(25) Sun, Y.; Welch, G. C.; Leong, W. L.; Takacs, C. J.; Bazan, G. C.; Heeger, A. J. Solution-Processed Small-Molecule Solar Cells with 6.7% Efficiency. *Nat. Mater.* **2011**, *11* (1), 44–48.

(26) Tang, C. W. Two-Layer Organic Photovoltaic Cell. *Appl. Phys. Lett.* **1986**, *48* (2), 183.

(27) Yu, G.; Gao, J.; Hummelen, J. C.; Wudl, F.; Heeger, A. J. Polymer Photovoltaic Cells: Enhanced Efficiencies via a Network of Internal Donor-Acceptor Heterojunctions. *Science (80-.).* **1995**, *270* (5243), 1789–1791.

(28) Heeger, A. J. 25th Anniversary Article: Bulk Heterojunction Solar Cells: Understanding the Mechanism of Operation. *Adv. Mater.* **2014**, *26* (1), 10–28.

(29) Hoppe, H.; Sariciftci, N. S. Organic Solar Cells: An Overview. *J. Mater. Res.* **2004**, *19* (07), 1924–1945.

(30) Thompson, B. C.; Fréchet, J. M. J. Polymer–Fullerene Composite Solar Cells. *Angew. Chemie Int. Ed.* **2008**, *47* (1), 58–77.

(31) Kim, Y.; Cook, S.; Tuladhar, S. M.; Choulis, S. A.; Nelson, J.; Durrant, J. R.; Bradley, D. D. C.; Giles, M.; McCulloch, I.; Ha, C.-S.; Ree, M. A Strong Regioregularity Effect in Self-Organizing Conjugated Polymer Films and High-Efficiency Polythiophene:fullerene Solar Cells. *Nat. Mater.* **2006**, *5* (3), 197–203.

(32) Li, G.; Shrotriya, V.; Yao, Y.; Yang, Y. Investigation of Annealing Effects and Film Thickness Dependence of Polymer Solar Cells Based on poly(3-Hexylthiophene). *J. Appl. Phys.* **2005**, *98* (4), 1–6.

(33) Clarke, T. M.; Ballantyne, A. M.; Nelson, J.; Bradley, D. D. C.; Durrant, J. R. Free Energy Control of Charge Photogeneration in Polythiophene/fullerene Solar Cells: The Influence of Thermal Annealing on P3HT/PCBM Blends. *Adv. Funct. Mater.* **2008**, *18* (24), 4029–4035.

(34) Li, G.; Shrotriya, V.; Huang, J.; Yao, Y.; Moriarty, T.; Emery, K.; Yang, Y. High-Efficiency Solution Processable Polymer Photovoltaic Cells by Self-Organization of Polymer Blends. *Nat. Mater.* **2005**, *4* (11), 864–868.

(35) Bansal, N.; Reynolds, L. X.; MacLachlan, A.; Lutz, T.; Ashraf, R. S.; Zhang, W.; Nielsen, C. B.; McCulloch, I.; Rebois, D. G.; Kirchartz, T.; Hill, M. S.; Molloy, K. C.; Nelson, J.; Haque, S. A. Influence of Crystallinity and Energetics on Charge Separation in Polymer-Inorganic Nanocomposite Films for Solar Cells. *Sci. Rep.* **2013**, *3*, 1531.

(36) Dayal, S.; Reese, M. O.; Ferguson, A. J.; Ginley, D. S.; Rumbles, G.; Kopidakis, N. The Effect of Nanoparticle Shape on the Photocarrier Dynamics and Photovoltaic Device Performance of Poly(3-hexylthiophene):CdSe Nanoparticle Bulk Heterojunction Solar Cells. *Adv. Funct. Mater.* **2010**, *20* (16), 2629–2635.

(37) Heinemann, M. D.; von Maydell, K.; Zutz, F.; Kolny-Olesiak, J.; Borchert, H.; Riedel, I.; Parisi, J. Photo-Induced Charge Transfer and Relaxation of Persistent Charge Carriers in Polymer/Nanocrystal Composites for Applications in Hybrid Solar Cells. *Adv. Funct. Mater.* **2009**, *19* (23), 3788–3795.

(38) Beek, W. J. E.; Wienk, M. M.; Kemerink, M.; Yang, X.; Janssen, A. J. Hybrid Zinc Oxide Conjugated Polymer Bulk Heterojunction Solar Cells. **2005**, 9505–9516.

(39) Noone, K. M.; Strein, E.; Anderson, N. C.; Wu, P.-T.; Jenekhe, S. A.; Ginger, D. S. Broadband Absorbing Bulk Heterojunction Photovoltaics Using Low-Bandgap Solution-Processed Quantum Dots. *Nano Lett.* **2010**, *10* (7), 2635–2639.

(40) Greenham, N.; Peng, X.; Alivisatos, A. Charge Separation and Transport in Conjugated-Polymer/semiconductor-Nanocrystal Composites Studied by Photoluminescence

Quenching and Photoconductivity. *Phys. Rev. B. Condens. Matter* **1996**, *54* (24), 17628–17637.

(41) Schrier, J.; Demchenko, D. O.; Wang, L.; Alivisatos, A. P. Optical Properties of ZnO / ZnS and ZnO / ZnTe Heterostructures for Photovoltaic Applications. *Nano Lett.* **2007**, *7* (8), 2377–2382.

(42) Gao, P. X.; Ding, Y.; Mai, W.; Hughes, W. L.; Lao, C.; Wang, Z. L. Conversion of Zinc Oxide Nanobelts into Superlattice-Structured Nanohelices. *Science (80-.).* **2005**, *309* (5741), 1700–1704.

(43) Van Hal, P. A.; Christiaans, M. P. T.; Wienk, M. M.; Kroon, J. M.; Janssen, R. A. J. Photoinduced Electron Transfer from Conjugated Polymers to TiO 2. *J. Phys. Chem. B* **1999**, *103* (21), 4352–4359.

(44) Shankar, K.; Mor, G. K.; Prakasam, H. E.; Varghese, O. K.; Grimes, C. A.; Pennsyl, T.; State, V.; Uni, V.; Park, U. V; Pennsyl, V. Self-Assembled Hybrid Polymer - TiO 2 Nanotube Array Heterojunction Solar Cells. *Langmuir* **2007**, *290* (13), 12445–12449.

(45) Liu, Y.; Scully, S. R.; McGehee, M. D.; Liu, J.; Luscombe, C. K.; Frechet, J. M. J.; Shaheen, S. E.; Ginley, D. S. 200. Dependence of Band Offset and Open-Circuit Voltage on the Interfacial Interaction between TiO2 and Carboxylated Polythiophenes BT - Journal of Physical Chemistry B. *J. Phys. Chem. B* **2006**, *110*, 3257–3261.

(46) Goh, C.; Scully, S. R.; McGehee, M. D. Effects of Molecular Interface Modification in Hybrid Organic-Inorganic Photovoltaic Cells. *J. Appl. Phys.* **2007**, *101* (11), 114503.

(47) Gerein, N. J.; Fleischauer, M. D.; Brett, M. J. Effect of TiO2 Film Porosity and Thermal Processing on TiO2–P3HT Hybrid Materials and Photovoltaic Device Performance. *Sol. Energy Mater. Sol. Cells* **2010**, *94* (12), 2343–2350.

(48) Min, C.; Li, J.; Veronis, G.; Lee, J. Y.; Fan, S.; Peumans, P. Enhancement of Optical Absorption in Thin-Film Organic Solar Cells through the Excitation of Plasmonic Modes in Metallic Gratings. *Appl. Phys. Lett.* **2010**, *96* (13).

(49) Xi, J.-Q.; Schubert, M. F.; Kim, J. K.; Schubert, E. F.; Chen, M.; Lin, S.-Y.; Liu, W.; Smart, J. A. Optical Thin-Film Materials with Low Refractive Index for Broadband Elimination of Fresnel Reflection. *Nat. Photonics* **2008**, *1* (3), 176–179.

(50) Brongersma, M. L.; Cui, Y.; Fan, S. Light Management for Photovoltaics Using High-Index Nanostructures. *Nat. Mater.* **2014**, *13* (5), 451–460.

(51) Polman, A. APPLIED PHYSICS: Plasmonics Applied. *Science (80-.).* **2008**, *322* (5903), 868–869.

(52) Ferry, V. E.; Munday, J. N.; Atwater, H. A. Design Considerations for Plasmonic Photovoltaics. *Adv. Mater.* **2010**, *22* (43), 4794–4808.

(53) Atwater, H. A.; Polman, A. Plasmonics for Improved Photovoltaic Devices. *Nat. Mater.* **2010**, *9* (3), 205–213.

(54) Wu, J.-L.; Chen, F.-C.; Hsiao, Y.-S.; Chien, F.-C.; Chen, P.; Kuo, C.-H.; Huang, M. H.; Hsu, C.-S. Surface Plasmonic Effects of Metallic Nanoparticles on the Performance of Polymer Bulk Heterojunction Solar Cells. *ACS Nano* **2011**, *5* (2), 959–967.

(55) Morfa, A. J.; Rowlen, K. L.; Reilly, T. H.; Romero, M. J.; van de Lagemaat, J. Plasmon-Enhanced Solar Energy Conversion in Organic Bulk Heterojunction Photovoltaics. *Appl. Phys. Lett.* **2008**, *92* (1), 013504.

(56) B. O'Reagan, M. G. A Low-Cost, High-Efficiency Solar Cell Based on Dye-Sensitized Colloidal TiO2 Films. *Nature* **1991**, *353*, 737–740.

(57) Guldin, S.; Hüttner, S.; Kolle, M.; Welland, M. E.; Müller-Buschbaum, P.; Friend, R. H.; Steiner, U.; Tétreault, N. Dye-Sensitized Solar Cell Based on a Three-Dimensional Photonic Crystal. *Nano Lett.* **2010**, *10* (7), 2303–2309.

(58) Chen, J. I. L.; von Freymann, G.; Choi, S. Y.; Kitaev, V.; Ozin, G. A. Amplified Photochemistry with Slow Photons. *Adv. Mater.* **2006**, *18* (14), 1915–1919.

(59) John, S.; Blanco, A.; Chomski, E.; Grabtchak, S.; Ibisate, M.; Leonard, S. W.; Lopez, C.; Meseguer, F.; Miguez, H.; Mondia, J. P.; Ozin, G. A.; Toader, O.; van Driel, H. M. No Title. *Nature* **2000**, *405* (6785), 437–440.

(60) Suezaki, T.; O'Brien, P. G.; Chen, J. I. L.; Loso, E.; Kherani, N. P.; Ozin, G. A. Tailoring the Electrical Properties of Inverse Silicon Opals - A Step Towards Optically Amplified Silicon Solar Cells. *Adv. Mater.* **2009**, *21* (5), 559–563.

(61) Suezaki, T.; Yano, H.; Hatayama, T.; Ozin, G. A.; Fuyuki, T. Photoconductivity in Inverse Silicon Opals Enhanced by Slow Photon Effect: Yet Another Step towards Optically Amplified Silicon Photonic Crystal Solar Cells. *Appl. Phys. Lett.* **2011**, *98* (7), 2009–2012.

(62) Suezaki, T.; Chen, J. I. L.; Hatayama, T.; Fuyuki, T.; Ozin, G. A. Electrical Properties of P-Type and N-Type Doped Inverse Silicon Opals - Towards Optically Amplified Silicon Solar Cells. *Appl. Phys. Lett.* **2010**, *96* (24), 0–3.

(63) Yablonovitch, E. Inhibited Spontaneous Emission in Solid-State Physics and Electronics. *Phys. Rev. Lett.* **1987**, *58* (20), 2059–2062.

(64) John, S. Strong Localization of Photons in Certain Disordered Dielectric Superlattices. *Phys. Rev. Lett.* **1987**, *58* (23), 2486–2489.

(65) Joannopoulos, J. D.; Villeneuve, P. R.; Fan, S. Photonic Crystals: Putting a New Twist on Light. *Nature* **1997**, *386* (6621), 143–149.

(66) Ozin, G. A.; Arsenault, A. C.; Cademartiri, L. *Nanochemistry: A Chemical Approach to Nanochemistry*, 2nd ed.; The Royal Society of Chemistry: Cambridge, 2009.

(67) Teyssier, J.; Saenko, S. V.; van der Marel, D.; Milinkovitch, M. C. Photonic Crystals Cause Active Colour Change in Chameleons. *Nat. Commun.* **2015**, *6*, 6368.

(68) Vukusic, P.; Sambles, J. R. Photonic Structures in Biology. *Nature* **2003**, *424* (6950), 852–855.

(69) Joannopoulos, J. J. D.; Johnson, S.; Winn, J. N. J.; Meade, R. R. D. *Photonic Crystals: Molding the Flow of Light*, 2nd ed.; Princeton University Press: New Jersey, 2008.

(70) Soljačić, M.; Joannopoulos, J. D. Enhancement of Nonlinear Effects Using Photonic Crystals. *Nat. Mater.* **2004**, *3* (4), 211–219.

(71) Hatton, B.; Mishchenko, L.; Davis, S.; Sandhage, K. H.; Aizenberg, J. Assembly of Large-Area, Highly Ordered, Crack-Free Inverse Opal Films. *Proc. Natl. Acad. Sci.* **2010**, *107* (23), 10354–10359.

(72) Vos, W. L.; Series, N.; Wijnhoven, J. E. Preparation of Photonic Crystals Made of Air Spheres in Titania. *Science (80-.).* **1998**, *281* (5378), 802–804.

(73) López, C. Materials Aspects of Photonic Crystals. *Adv. Mater.* **2003**, *15* (20), 1679–1704.

(74) Nishimura, S.; Abrams, N.; Lewis, B. a; Halaoui, L. I.; Mallouk, T. E.; Benkstein, K. D.; van de Lagemaat, J.; Frank, A. J. Standing Wave Enhancement of Red Absorbance and Photocurrent in Dye-Sensitized Titanium Dioxide Photoelectrodes Coupled to Photonic Crystals. *J. Am. Chem. Soc.* **2003**, *125* (20), 6306–6310.

(75) Chen, J. I. L.; von Freymann, G.; Choi, S. Y.; Kitaev, V.; Ozin, G. A. Slow Photons in the Fast Lane in Chemistry. *J. Mater. Chem.* **2008**, *18* (4), 369.

(76) Baba, T. Slow Light in Photonic Crystals. *Nat. Photonics* **2008**, *2* (8), 465–473.

(77) Shouldice, G. T. D.; Vandezande, G. A.; Rudin, A. Practical Aspects of the Emulsifier-Free Emulsion Polymerization of Styrene. *Eur. Polym. J.* **1994**, *30* (2), 179–183.

(78) Jiang, P.; Bertone, J. F.; Hwang, K. S.; Colvin, V. L. Single-Crystal Colloidal Multilayers of Controlled Thickness. *Chem. Mater.* **1999**, *11* (8), 2132–2140.

(79) Von Freymann, G.; John, S.; Wong, S.; Kitaev, V.; Ozin, G. A. Measurement of Group Velocity Dispersion for Finite Size Three-Dimensional Photonic Crystals in the near-Infrared Spectral Region. *Appl. Phys. Lett.* **2005**, *86* (5), 1–3.

(80) Mittleman, D. M.; Bertone, J. F.; Jiang, P.; Hwang, K. S.; Colvin, V. L. Optical Properties of Planar Colloidal Crystals: Dynamical Diffraction and the Scalar Wave Approximation. *J. Chem. Phys.* **1999**, *111* (1), 345.

(81) Galisteo-López, J. F.; Palacios-Lidón, E.; Castillo-Martínez, E.; López, C. Optical Study of the Pseudogap in Thickness and Orientation Controlled Artificial Opals. *Phys. Rev. B* **2003**, *68* (11), 115109.

(82) Von Freymann, G.; John, S.; Schulz-Dobrick, M.; Vekris, E.; Tétreault, N.; Wong, S.; Kitaev, V.; Ozin, G. A. Tungsten Inverse Opals: The Influence of Absorption on the Photonic Band Structure in the Visible Spectral Region. *Appl. Phys. Lett.* **2004**, *84* (2), 224.

(83) Shrotriya, V.; Ouyang, J.; Tseng, R. J.; Li, G.; Yang, Y. Absorption Spectra Modification in poly(3-Hexylthiophene):methanofullerene Blend Thin Films. *Chem. Phys. Lett.* **2005**, *411* (1-3), 138–143.

(84) Na, J. Y.; Kang, B.; Sin, D. H.; Cho, K.; Park, Y. D. Understanding Solidification of Polythiophene Thin Films during Spin-Coating: Effects of Spin-Coating Time and Processing Additives. *Sci. Rep.* **2015**, *5* (April), 13288.

(85) Cook, S.; Furube, A.; Katoh, R. Analysis of the Excited States of Regioregular Polythiophene P3HT. *Energy Environ. Sci.* **2008**, *1* (2), 294.

(86) Woo, C. H.; Thompson, B. C.; Kim, B. J.; Toney, M. F.; Fréchet, J. M. J. The Influence of poly(3-Hexylthiophene) Regioregularity on Fullerene-Composite Solar Cell Performance. *J. Am. Chem. Soc.* **2008**, *130* (48), 16324–16329.

(87) Spano, F. C.; Silva, C. H- and J-Aggregate Behavior in Polymeric Semiconductors. *Annu. Rev. Phys. Chem.* **2014**, *65* (1), 477–500.

(88) Clark, J.; Silva, C.; Friend, R. H.; Spano, F. C. Role of Intermolecular Coupling in the Photophysics of Disordered Organic Semiconductors: Aggregate Emission in Regioregular Polythiophene. *Phys. Rev. Lett.* **2007**, *98* (20), 1–4.

(89) Boschloo, G.; Hagfeldt, A. Photoinduced Absorption Spectroscopy as a Tool in the Study of Dye-Sensitized Solar Cells. *Inorganica Chim. Acta* **2008**, *361* (3), 729–734.

(90) Dellepiane, G.; Cuniberti, C.; Comoretto, D.; Musso, G. F.; Figari, G.; Piaggi, A.; Borghesi, A. Long-Lived Photoexcited States in Symmetrical Polydicarbazolyldiacetylene. *Phys. Rev. B* **1993**, *48* (11), 7850–7856.

(91) Epshtein, O.; Nakhmanovich, G.; Eichen, Y.; Ehrenfreund, E. Dispersive Dynamics of Photoexcitations in Conjugated Polymers Measured by Photomodulation Spectroscopy. *Phys. Rev. B* **2001**, *63* (12), 2–7.

(92) Smilowitz, L.; Sariciftci, N. S.; Wu, R.; Gettinger, C.; Heeger, a. J.; Wudl, F. Photoexcitation Spectroscopy of Conducting-Polymer-C60 Composites: Photoinduced Electron Transfer. *Phys. Rev. B* **1993**, *47* (20), 13835–13842.

(93) Nogueira, A. F.; Montanari, I.; Nelson, J.; Durrant, J. R.; Winder, C.; Sariciftci, N. S. Charge Recombination in Conjugated Polymer/fullerene Blended Films Studied by Transient Absorption Spectroscopy. *J. Phys. Chem. B* **2003**, *107*, 1567–1573.

(94) Cappel, U. B.; Gibson, E. A.; Hagfeldt, A.; Boschloo, G. Dye Regeneration by Spiro-MeOTAD in Solid State Dye-Sensitized Solar Cells Studied by Photoinduced Absorption Spectroscopy and Spectroelectrochemistry. *J. Phys. Chem. C* **2009**, *113* (15), 6275–6281.

(95) Brédas, J. L.; Wudl, F.; Heeger, A. J. Polarons and Bipolarons in Doped Polythiophene: A Theoretical Investigation. *Solid State Commun.* **1987**, *63* (7), 577–580.

(96) Zhang, W.; Heeney, M.; McCulloch, I.; Nelson, J.; Bradley, D. D. C.; Durrant, J. R.; Ohkita, H.; Cook, S.; Astuti, Y.; Duffy, W.; Tierney, S. Charge Carrier Formation in Polythiophene/fullerene Blend Films Studied by Transient Absorption Spectroscopy. *J. Am. Chem. Soc.* **2008**, *130* (10), 3030–3042.

(97) Brown, P. J.; Sirringhaus, H.; Harrison, M.; Shkunov, M.; Friend, R. H. Optical Spectroscopy of Field-Induced Charge in Self-Organized High Mobility poly(3-Hexylthiophene). *Phys. Rev. B* **2001**, *63* (12), 125204.

(98) Gelinas, S.; Rao, A.; Kumar, A.; Smith, S. L.; Chin, A. W.; Clark, J.; van der Poll, T. S.; Bazan, G. C.; Friend, R. H. Ultrafast Long-Range Charge Separation in Organic Semiconductor Photovoltaic Diodes. *Science (80-.).* **2014**, *343* (6170), 512–516.

(99) Noone, K. M.; Subramaniyan, S.; Zhang, Q.; Cao, G.; Jenekhe, S. A.; Ginger, D. S. Photoinduced Charge Transfer and Polaron Dynamics in Polymer and Hybrid Photovoltaic Thin Films : Organic vs Inorganic Acceptors. *J. Phys. Chem. C.* **2011**, *115*, 24403–24410.

(100) Noone, K. M.; Anderson, N. C.; Horwitz, N. E.; Munro, A. M.; Kulkarni, A. P.; Ginger, D. S. Absence of Photoinduced Charge Transfer in Blends of PbSe Quantum Dots and Conjugated Polymers. *ACS Nano* **2009**, *3* (6), 1345–1352.

(101) Osterbacka, R.; An, C. P.; Jiang, X. M.; Vardeny, Z. V. Two-Dimensional Electronic Excitations in Self-Assembled Conjugated Polymer Nanocrystals. *Science (80-.).* **2000**, *287* (5454), 839–842.

(102) Wei, X.; Vardeny, Z.; Sariciftci, N.; Heeger, A. Absorption-Detected Magnetic-Resonance Studies of Photoexcitations in Conjugated-polymer/C60 Composites. *Phys. Rev. B* **1996**, *53* (5), 2187–2190.

(103) Marsh, R. A.; Hodgkiss, J. M.; Albert-Seifried, S.; Friend, R. H. Effect of Annealing on P3HT:PCBM Charge Transfer and Nanoscale Morphology Probed by Ultrafast Spectroscopy. *Nano Lett.* **2010**, *10* (3), 923–930.

(104) Yoshihara, T.; Yoshihara, T.; Katoh, R.; Katoh, R.; Furube, A.; Furube, A.; Tamaki, Y.; Tamaki, Y.; Murai, M.; Murai, M.; Hara, K.; Hara, K.; Murata, S.; Murata, S.; Arakawa, H.; Arakawa, H. Identification of Reactive Species in Photoexcited Nanocrystalline TiO 2 Films by Wide-Wavelength-Range (400−2500 Nm) Transient Absorption Spectroscopy. *J. Phys. Chem. B* **2004**, *108* (12), 3817–3823.

(105) Szczepankiewicz, S. H.; Moss, J. A.; Hoffmann, M. R. Slow Surface Charge Trapping Kinetics on Irradiated TiO2. *J. Phys. Chem. B* **2002**, *106* (11), 2922–2927.

(106) Panayotov, D. A.; Burrows, S. P.; Morris, J. R. Infrared Spectroscopic Studies of Conduction Band and Trapped Electrons in UV-Photoexcited, H-Atom N-Doped, and Thermally Reduced TiO 2. *J. Phys. Chem. C* **2012**, *116* (7), 4535–4544.

(107) Yamakata, A.; Ishibashi, T. A.; Onishi, H. Time-Resolved Infrared Absorption Spectroscopy of Photogenerated Electrons in Platinized TiO2 Particles. *Chem. Phys. Lett.* **2001**, *333* (3-4), 271–277.

(108) Di Valentin, C.; Pacchioni, G.; Selloni, A. Reduced and N-Type Doped TiO 2 : Nature of Ti 3+ Species. *J. Phys. Chem. C* **2009**, *113* (48), 20543–20552.